University of Kentucky
UKnowledge

Theses and Dissertations--Physics and Astronomy

Physics and Astronomy

2017

DECONFINED QUANTUM CRITICALITY IN 2D SU(N) MAGNETS WITH ANISOTROPY

Jonathan D'Emidio
University of Kentucky, jonathan.demidio@uky.edu

Digital Object Identifier: https://doi.org/10.13023/ETD.2017.420

Right click to open a feedback form in a new tab to let us know how this document benefits you.

Recommended Citation

D'Emidio, Jonathan, "DECONFINED QUANTUM CRITICALITY IN 2D SU(N) MAGNETS WITH ANISOTROPY" (2017). *Theses and Dissertations--Physics and Astronomy*. 50.
https://uknowledge.uky.edu/physastron_etds/50

This Doctoral Dissertation is brought to you for free and open access by the Physics and Astronomy at UKnowledge. It has been accepted for inclusion in Theses and Dissertations--Physics and Astronomy by an authorized administrator of UKnowledge. For more information, please contact UKnowledge@lsv.uky.edu.

STUDENT AGREEMENT:

I represent that my thesis or dissertation and abstract are my original work. Proper attribution has been given to all outside sources. I understand that I am solely responsible for obtaining any needed copyright permissions. I have obtained needed written permission statement(s) from the owner(s) of each third-party copyrighted matter to be included in my work, allowing electronic distribution (if such use is not permitted by the fair use doctrine) which will be submitted to UKnowledge as Additional File.

I hereby grant to The University of Kentucky and its agents the irrevocable, non-exclusive, and royalty-free license to archive and make accessible my work in whole or in part in all forms of media, now or hereafter known. I agree that the document mentioned above may be made available immediately for worldwide access unless an embargo applies.

I retain all other ownership rights to the copyright of my work. I also retain the right to use in future works (such as articles or books) all or part of my work. I understand that I am free to register the copyright to my work.

REVIEW, APPROVAL AND ACCEPTANCE

The document mentioned above has been reviewed and accepted by the student’s advisor, on behalf of the advisory committee, and by the Director of Graduate Studies (DGS), on behalf of the program; we verify that this is the final, approved version of the student’s thesis including all changes required by the advisory committee. The undersigned agree to abide by the statements above.

Jonathan D'Emidio, Student

Dr. Ribhu K. Kaul, Major Professor

Dr. Christopher Crawford, Director of Graduate Studies

DECONFINED QUANTUM CRITICALITY IN 2D SU(N) MAGNETS WITH ANISOTROPY

DISSERTATION

A dissertation submitted in partial
fulfillment of the requirements for
the degree of Doctor of Philosophy
in the College of Arts and Sciences
at the University of Kentucky

By
Jonathan D'Emidio
Lexington, Kentucky

Director: Dr. Ribhu K. Kaul, Professor of Physics
Lexington, Kentucky 2017

Copyright© Jonathan D'Emidio 2017

ABSTRACT OF DISSERTATION

DECONFINED QUANTUM CRITICALITY IN 2D SU(N) MAGNETS WITH ANISOTROPY

In this thesis I will outline various quantum phase transitions in 2D models of magnets that are amenable to simulation with quantum Monte Carlo techniques. The key player in this work is the theory of deconfined criticality, which generically allows for zero temperature quantum phase transitions between phases that break distinct global symmetries. I will describe models with different symmetries including SU(N), SO(N), and "easy-plane" SU(N) and I will demonstrate how the presence or absence of continuous transitions in these models fits together with the theory of deconfined criticality.

KEYWORDS: SU(N), SO(N), Quantum Magnetism, Quantum Phase Transitions, Deconfined Criticality, Quantum Monte Carlo

Author's signature: Jonathan D'Emidio

Date: October 23, 2017

DECONFINED QUANTUM CRITICALITY IN 2D SU(N) MAGNETS WITH ANISOTROPY

By
Jonathan D'Emidio

Director of Dissertation: Ribhu K. Kaul

Director of Graduate Studies: Christopher Crawford

Date: October 23, 2017

To mom and dad, Nick and Erica, Grandmom and Nan.

ACKNOWLEDGMENTS

I would like to thank my high school physics teachers, David Bender and Hank Oppenheimer (Opp). Without their passion and encouragement, my lifelong interest in physics may have never been sparked. I am grateful that I met Joshua Melko and other graduate students at Penn State. They made graduate school look fun and encouraged me to pursue it. I was fortunate to meet so many wonderful graduate students at the University of Kentucky. I would like to thank Diptarka Das (Dip), Raza Sabbir Sufian (Sabbir), Mathias Boland, Kyle McCarthy, John Gruenewald, Mirza Sharoz Rafiul Islam (Sharoz) and many others. I thank Ganpathy Murthy for showing me the beauty of condensed matter physics. I am forever grateful to Ribhu Kaul for believing in me, and for allowing me to pursue such an exciting area of physics research.

TABLE OF CONTENTS

LIST OF TABLES

LIST OF FIGURES

Chapter 1 Introduction

1.1 Historical Perspective

Magnetism has fascinated human beings for centuries, given the presence of naturally occurring permanent magnets called lodestone [4]. The ability of these rocks to push or pull on each other from a distance must have been an incredibly magical curiosity to early civilizations. It is undeniable, however, that the curious trick that these rocks play would eventually give rise to one of the most revolutionary instruments in the ancient world and one that we still use today: the compass.

Fast forward to the early 1800's where we find that the compass helped to cause yet another revolution, this time in our understanding of fundamental physics. While giving a lecture demonstration at the University of Copenhagen, Hans Christian Ørsted noticed by accident the twitching of a compass needle sitting near an active electrical wire [5]. Thus sparked the chain of events that led to our understanding of two seemingly unrelated phenomena, culminating in the unified theory of electromagnetism developed by Maxwell in the years 1860-1871.

Although ferromagnetism has been known for thousands of years, only within the past century has the phenomenon of antiferromagnetism been discovered. This idea, pioneered by Louis Néel in the 1930's, was put forth in order to explain anomalous features of the low temperature magnetic susceptibility in certain materials [6]. Néel's idea of the "generalized ferromagnet" consisted of two inter-penetrating sublattices with opposite magnetization. With this theory he was able to correctly predict a peak in the temperature dependent susceptibility at the onset of antiferromagnetic order, now called the Néel temperature.

The quantum theory of antiferromagnetism found itself on shaky ground, as the quantum spin Hamiltonians thought to describe them (what we now call Heisenberg antiferromagnets) did not have the Néel state as an exact ground state. This called into question the ability for this state to form in a real material. It was only after the advent of neutron scattering, which was able to resolve the spin structure of MnO crystals, that clear peaks corresponding to Néel order emerged [6].

For the same reason that antiferromagnetism seemed implausible, namely the presence of strong quantum fluctuations, it is now at the forefront of some of the most exciting areas of condensed matter physics. High temperature superconductors have antiferromagnetic insulators as their parent compounds [7]. Upon doping these systems with mobile charge carriers, one encounters many exotic phases that defy conventional wisdom and it is believed that antiferromagnetic correlations play an intimate role. Even the antiferromagnetic insulators themselves can show bizarre properties, when for instance one considers geometrically frustrated lattices such as the kagome. Here the quantum fluctuations of the spins can be so large that the system becomes completely disordered yet highly entangled. Such is the case for so-called quantum “spin-liquid” states, which can often give rise to non-trivial topological phenomena [8].

We can therefore draw a parallel to the discovery of ferromagnetism in the time of antiquity, a curiosity that would eventually lead to a revolution in technology. In the current age we are in the midst of discovering all of the curiosities associated with antiferromagnetism. It may well be that out of this process of discovery, we may see great technological revolutions such as room temperature superconductors or topological quantum computers. The even more exciting prospect however, is the chance for these possible technologies to do what the compass had done for the discovery of electromagnetism, and reveal to us new fundamental truths about the nature of reality.

1.2 Deconfined Quantum Criticality

From a theoretical perspective, a fruitful route to the discovery of new and interesting quantum mechanical phenomena is to start from the antiferromagnetically ordered Néel state and try to disorder it [9]. This is typically done by adding extra terms to the Heisenberg Hamiltonian:

$$H = J \sum_{\langle ij \rangle} \vec{S}_i \cdot \vec{S}_j + ... \tag{1.1}$$

Here the spin operators are matrices, which generate the group SU(2). Global unitary SU(2) transformations of all of the spin operators (spins) leaves the Hamiltonian invariant and the model is said to have SU(2) symmetry. Here the sum over $\langle ij \rangle$ corresponds to nearest neighbor interactions. If we take this model on a two dimensional bipartite lattice, the ground state has long range Néel order. However, as previously mentioned, quantum fluctuations serve to reduce the staggered magnetization as compared with the perfect Néel state.

We now wish to add an extra SU(2) symmetric interaction to the Hamiltonian in the hopes of destroying the Néel state. If we consider the case of the 2D square lattice, one particularly interesting interaction consists of a product of two Heisenberg nearest neighbor terms acting alongside one another on an elementary plaquette [10].

$$H_{JQ} = J \sum_{\langle ij \rangle} \vec{S}_i \cdot \vec{S}_j - Q \sum_{\langle ijkl \rangle} \left(\vec{S}_i \cdot \vec{S}_j - \frac{1}{4} \right) \left(\vec{S}_k \cdot \vec{S}_l - \frac{1}{4} \right) \tag{1.2}$$

It is this model that forms the foundation of the work that is to be presented in the rest of this thesis. In order to discuss the significance of this model, we must first discuss the nature of the ground state when $J = 0$ and only the Q term exists. In this limit the Néel order of the spins is completely destroyed, and the ground state preserves the global SU(2) symmetry of the Hamiltonian. Such a ground state is composed of spin-0 singlets, where the singlet wave function for two spins is written as $\frac{1}{\sqrt{2}} (| \uparrow\downarrow \rangle - | \downarrow\uparrow \rangle)$. Neighboring spins are paired up into singlets in such a way that

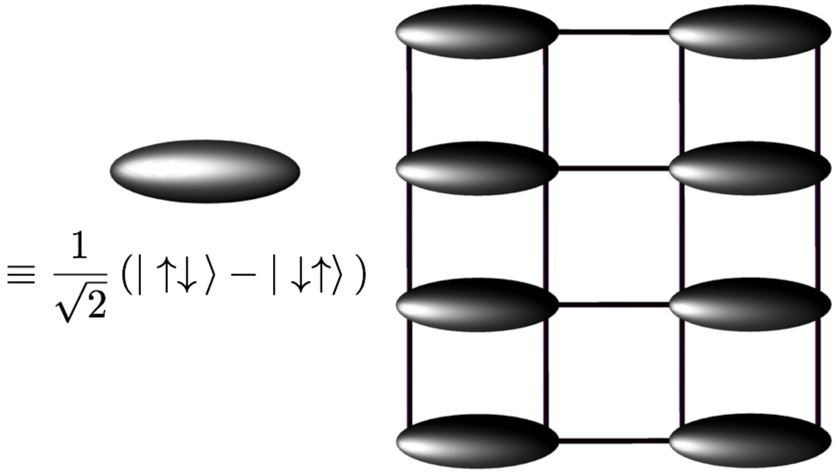

Figure 1.1: A cartoon picture of the columnar valence bond solid (VBS) state on the square lattice. Valence bonds correspond to singlets of adjacent spins, represented by the blobs. This state preserves the spin rotational symmetry of the J-Q Hamilonian but breaks lattice translational symmetry.

they form a regular pattern on the square lattice, known as the columnar “valence-bond solid” (VBS) state. A cartoon of the VBS state is given in Fig. 1.1.

The important thing about the VBS state is that it preserves the spin rotational symmetry of the Hamiltonian, but it breaks the lattice translational symmetry. In contrast, the Néel state breaks spin rotational symmetry but preserves lattice translational symmetry (the staggered magnetization is spatially uniform).

A very important fact about the J-Q model is that it is amenable to very efficient numerical simulations based on the quantum Monte Carlo (QMC) method [11,12]. A notable example of a QMC algorithm that is typically employed to tackle problems of this nature, and one that is used throughout the work in this thesis, is called the stochastic series expansion (SSE) algorithm (see [13] for an excellent exposition). The ability to avoid the sign problem and apply efficient algorithms such as these means that large scale numerical simulations have been extensively carried out on this model. The result is a continuous phase transition as a function of Q/J from the Néel phase to the VBS phase [10].

This fact immediately poses a problem from the point of view of conventional phase transitions of the kind envisioned by Landau, Ginzburg [14] and Wilson [15] (LGW). The normal way that phase transitions are described in this context, is by fluctuations of an order parameter field. In the case of the *J*-*Q* model there are seemingly two very different order parameters, one describing Néel order and the other VBS order. A standard treatment of the phase transition, if one requires the Néel to VBS transition to be direct, would generically lead to a first order transition. Thus the LGW paradigm cannot give a natural description of the direct, continuous transition from Néel to VBS where just one parameter is tuned.

The theory of deconfined quantum criticality [16, 17] has been constructed with this problem explicitly in mind. It says that instead of considering the Néel field (the local staggered magnetization) as the fundamental object out of which we build an energy functional, let's instead treat it as a composite object. This can formally be accomplished by making use the $\mathbb{CP}^1$ parametrization of the unit sphere, where if $\hat{n}$ is a unit vector representing the local Néel field, it can be written as

$$\hat{n} = z^\dagger \vec{\sigma} z, \tag{1.3}$$

Where here z is a function of space and imaginary time, $z = z(\vec{r}, \tau)$, and is a two component object, $z = (z_1, z_2)^\intercal$, where at any coordinate each component is a complex number. Since the Néel vector is taken to have unit magnitude, we also have the constraint that $|z_1|^2 + |z_2|^2{=}1$.

A very important aspect of rewriting the problem in this way is that there is a local gauge redundancy of the z fields, meaning sending $z \to e^{i\gamma(\vec{r},\tau)} z$ represents the same configuration of the Néel field. In order to enforce this equivalence, the z-fields are then coupled to a compact U(1) gauge field. The central result of deconfined criticality is that the compactness of the gauge field can be neglected exactly at the critical point. The theory describing the transition is then the non-compact $\mathbb{CP}^1$ field theory, which is the simplest theory of complex scalar fields coupled to a U(1) gauge field.

Throughout the work in this thesis we will be concerned with the connection between the $\mathbb{CP}^1$ theory and its connection with criticality in lattice models. More generally we will be interested in the $\mathbb{CP}^{N-1}$ theory and the SU(N) magnetic to VBS transitions, as well as symmetry deformations to these models.

1.3 Outline of Thesis

In Chapter 2 we will introduce the SU(N) symmetric spin models that give rise to deconfined magnetic-VBS phase transitions for arbitrary integer values of $N \geq 5$. We will then use this model at $N = 10$ to extract the scaling behavior of the spin stiffness (a measure of magnetic order) at the critical point to show that we find conventional critical scaling there. This is in stark contrast the the $N = 2$ J-Q model where anomalous scaling is observed [2].

In Chapter 3 we will consider a variant of the model introduced in Chapter 2, except on a different lattice that allows for the addition of SO(N) spin anisotropy. The central question there is with regard to the stability of the deconfined critical point in the SU(N) models in the presence of SO(N) anisotropy. We then go on to explore the whole phase diagram of the SO(N) model, which includes an interesting spin liquid phase.

In Chapter 4 we introduce what we call "easy-plane" SU(N) anisotropy into these models, which is equivalent to considering multicomponent superfluid to VBS transitions. We find that in our small N model the transition is always first order, meaning that the SU(N) symmetric deconfined critical point is unstable to the presence of this type of anisotropy at small N.

Finally, in Chapter 5 we introduce a model with the same "easy-plane" SU(N) anisotropy, except that it realizes the superfluid to VBS transition at large N. Here we find that beyond a critical value of $N \approx 20$, the first-order transition becomes continuous. This conclusion is supported by performing renormalization group calculations on a $\mathbb{CP}^{N-1}$ field theory with easy-plane anisotropy added.

The Vita at the end of the dissertation gives a complete list of projects that I have worked on during my Ph.D. residency at the University of Kentucky. This includes the projects that have led to publications, as well as projects that are to be published in the near future. A subset of this work forms the chapters in this thesis.

Chapter 2 Deconfined Criticality in SU(N) Magnets at Large N

2.1 Introduction

As we have previously mentioned, the J-Q model [10] is the prototypical example of a simple spin Hamiltonian whose physics, in terms of the nature of the transition from Néel to VBS states, lies outside the LGW paradigm [17]. It is also a model that is amenable to highly efficient quantum Monte Carlo algorithms [11,12], which have allowed for an extremely detailed analysis of the critical properties of the transition.

This detailed analysis has revealed anomalous critical behavior, as is observed in unconventional finite sized scaling behavior at the transition [18]. This has resulted in controversy over the possibility of first-order behavior [19,20], as well as alternative scaling forms including the potential for two diverging length scales [2].

This anomalous behavior motivates a closer investigation of lattice models of deconfined criticality at large N. Along these lines, the natural starting point is the SU(N) symmetric spin model that very naturally realizes deconfined criticality for higher values of $N > 2$ [1]. This class of models includes the SU(N) symmetric J-Q and J_1-J_2 models, the latter being the focus of this chapter. Here we will introduce the J_1-J_2 model and discuss the measurement of the spin stiffness (ρ_s) in this model and how this measurement behaves anomalously in the $N = 2$ case at the transition. We will then go on to examine this quantity with high accuracy for $N = 10$, eventually showing that conventional quantum critical scaling is recovered in this case.

2.2 Lattice Model

Here we introduce the Hamiltonian that will allow us to gain access to the deconfined magnetic to VBS phase transition at large N. The Hamiltonian can very simply be written as a sum of two terms [21]:

$$H_{\mathrm{SU}(N)} = -\frac{J_1}{N}\sum_{\langle ij\rangle} P_{ij} - \frac{J_2}{N}\sum_{\langle\langle ij\rangle\rangle} \Pi_{ij}, \tag{2.1}$$

where $P_{ij} = \sum_{\alpha,\beta} |\alpha_i\alpha_j\rangle\langle\beta_i\beta_j|$ is the projection operator onto the two-site SU(N) singlet in the staggered representation, and $\Pi_{ij} = \sum_{\alpha,\beta} |\alpha_i\beta_j\rangle\langle\beta_i\alpha_j|$ is a permutation. The projection takes place on nearest-neighbor bonds of a square lattice ($\langle ij\rangle$) and the permutation is on next-nearest neighbors ($\langle\langle ij\rangle\rangle$).

This Hamiltonian has SU(N) symmetry, and can be written in terms of the generators of SU(N) if we choose the representation where we take the fundamental generators on one sublattice and the conjugate to the fundamental on the other sublattice [22]:

$$H_{\mathrm{SU}(N)} = -J_1\sum_{\langle ij\rangle} \vec{T}_i\cdot\vec{T}_j^* - J_2\sum_{\langle\langle ij\rangle\rangle} \vec{T}_i\cdot\vec{T}_j, \tag{2.2}$$

A crucial aspect about this model is that one can create an SU(N) singlet using just two neighboring sites, irrespective of the value of N. Furthermore, for $N = 2$ this model (up to a constant shift) is equivalent to the SU(2) Heisenberg model with an antiferromagnetic coupling on nearest-neighbor sites, and ferromagnetic coupling on next-nearest-neighbor sites (assuming $J_1, J_2 > 0$). This model is therefore very well motivated from the point of view of extending the physics of magnetic to VBS transitions to larger N.

This model, and variants of it have been heavily studied in the context of deconfined criticality (see [23] for a review of the literature), thus the extended phase diagram is already completely known. For the particular Hamiltonian that we work with here, it is known that for $J_2 = 0$, magnetic order persists up to and including $N = 4$ and columnar VBS order is present for $N \geq 5$.

The introduction of the J_2 term, which ferromagnetically couples spins on the same sublattice, encourages magnetic order. Thus by starting in the VBS phase and increasing J_2/J_1, one can tune from the VBS to the magnetic phase. This allows access to the phase transition for all values of $N \geq 5$.

2.3 Spin Stiffness

In this particular study we will exclusively focus on measurements of the spin stiffness (ρ_s), which can be computed in terms of the average winding number fluctuations in our QMC configurations (see [13] for the details of this measurement). Here we will briefly describe this quantity, and how it can be measured for SU(N) symmetric spin systems.

Firstly, in a magnetically ordered phase, we expect the spins to be ridgedly oriented with respect to one another. In such a phase, if we performed an incrementally increasing twist of the spins about some axis, the ground state energy would increase. Of course performing a unitary transformation incrementally to each spin would leave the energy unchanged, so what we really need is a twist of boundary conditions, equivalent to threading a magnetic flux through the system.

In order to accomplish this, we consider twisting by ϕ about a diagonal generator (S^{z} in the SU(2) case), in which case the spin operators get modified as follows: $S^+ \rightarrow S^+ e^{i\phi}, S^- \rightarrow S^- e^{-i\phi}$. In terms of bond operators we have $S_i^{\mathrm{z}} S_{i+1}^{\mathrm{z}} \rightarrow S_i^{\mathrm{z}} S_{i+1}^{\mathrm{z}}, S_i^+ S_{i+1}^+ \rightarrow S_i^+ S_{i+1}^+ e^{i\phi}, S_i^- S_{i+1}^- \rightarrow S_i^- S_{i+1}^- e^{-i\phi}$. Here we have used the fact that site i is in the fundamental representation and site $i+1$ is in the conjugate to the fundamental. Also we have assumed that site $i+1$ has been twisted by an amount ϕ more than site i.

Since we have the staggered the representation on the A and B sites, the phase factor changes depending on whether the site i is on an A site or a B site. In the SU(N) case, phase factors are associated with a particular "color," for instance color=$\bigcirc$, so that matrix elements are modified to

$$|\alpha_{\mathrm{A}}\alpha_{\mathrm{B}}\rangle\langle\bigcirc_{\mathrm{A}}\bigcirc_{\mathrm{B}}| \rightarrow |\alpha_{\mathrm{A}}\alpha_{\mathrm{B}}\rangle\langle\bigcirc_{\mathrm{A}}\bigcirc_{\mathrm{B}}|e^{-i\phi}. \tag{2.3}$$

Here the phase factor is 1 if $\alpha = \bigcirc$. A and B refer to the sublattice, and the conjugate phase factor is used when connecting from a B site to an A site.

The J_2 term has matrix elements of the form

$$|\alpha_{\mathrm{A}}\bigcirc_{\mathrm{A}}\rangle\langle\bigcirc_{\mathrm{A}}\alpha_{\mathrm{A}}| \rightarrow |\alpha_{\mathrm{A}}\bigcirc_{\mathrm{A}}\rangle\langle\bigcirc_{\mathrm{A}}\alpha_{\mathrm{A}}|e^{-i\phi}. \tag{2.4}$$

Where again there is no phase factor when $\alpha = \bigcirc$, and the conjugate phase factor is used when connecting from B site to B site. It can be shown that this is equivalent to twisting about the $N-1^{\mathrm{th}}$ diagonal generator of SU(N).

With this prescription, one can calculate the stiffness on small system sizes by exactly diagonalizing the Hamiltonian. In terms of the behavior of the ground state energy as a function of ϕ, the stiffness is given by

$$\rho_s = \left.\frac{\partial^2 E_0(\phi)}{\partial\phi^2}\right|_{\phi=0}. \tag{2.5}$$

This quantity can also be measured efficiently in the context of QMC [13], which amounts to computing “winding numbers” of the configurations. These winding numbers can be calculated easily for a given SSE configuration by simply looking at the bond operators (matrix elements) sequentially at each time slice. The displacement associated with the $\bigcirc$ color is incremented (decremented) each time one encounters an operator associated with a positive (negative) phase factor. The winding number in a particular spatial direction is then calculated as the total displacement in that direction divided by the linear system size in that direction. Winding numbers for

N	L_x	L_y	J_1	J_2	ED:e	QMC:e	ED:ρ_x	QMC:ρ_x
2	4	4	1.	1.	-2.164574915	-2.16465 (±4)	8.163880257	8.164 (±5)
3	4	2	1.	1.	-1.755860274	-1.7559 (±8)	2.074699044	2.0737 (±9)

Table 2.1: A table comparing the values of the energy per site (e), and the spin stiffness in the x-direction (ρ_{x}) obtained both from exactly diagonalizing the Hamiltonian with phase factors (ED) and with QMC. We see that for these two system sizes, for both SU(2) and SU(3), the QMC value agrees with exact diagonalization within the error bar.

each color and spatial direction are separately computed, then averaged. In terms of the winding number (W), the stiffness is given by

$$\rho_s = \frac{\langle W^2 \rangle}{\beta}, \tag{2.6}$$

where β is the inverse temperature. To show the agreement between exact diagonalization and QMC we show in Table 2.1 a comparison of the values of the energy per site (e) and the spin stiffness in the x-direction (ρ_{x}) for two different small system sizes.

The motivation for studying the scaling of the stiffness in this model is the following: one expects that at a continuous phase transition that the stiffness should scale as [24, 25] $\rho_s \propto L^{-(d+z-2)}$, where d is the spatial dimension and z is the dynamical critical exponent. z is usually taken to be one in the type of continuous transitions that we are concerned with here, meaning that we would expect $\rho_s \propto L^{-1}$ and so $L\rho_s$ should go to a constant at a continuous transition in our model.

It has however been observed that for the $N = 2$ Néel to VBS deconfined transition, $L\rho_s$ actually diverges slowly with a power less than one [18, 19, 26, 27]. This has sparked controversy about the possibility of a first-order transition [19, 20], however the resolution may be a modified scaling form of the stiffness due to the presence of two diverging length scales [2]. It is therefore the goal of this present study to examine the scaling behavior at the transition at larger N, in the hopes of establishing whether one recovers more conventional critical behavior or not. To this end we will pursue a study of the stiffness near the transition at $N = 10$ in our model and perform numerical fits in order to extract the scaling behavior.

2.4 Numerical Results

Our entire numerical analysis here will consist of analyzing the the crossing points of the quantity $L\rho_s$ for different sized LxL lattices across the VBS to magnetic transition in our SU(N) model. Due to the quantity and accuracy of the data that is required for this careful scaling analysis, we will focus our efforts on just one value of N ($N = 10$), with the intent of extending the scope of our study in the future.

Deep in the magnetic phase, the spin stiffness (properly normalized) should saturate to a constant as a function of system size. While, on the VBS side it goes to zero. This implies that the $L\rho_s$ curves will show a crossing for different system sizes near the transition. It is exactly these crossing points that we will use to study the scaling behavior of the stiffness at the transition. In particular we will consider the crossing points of $L\rho_s$ for pairs of system sizes (L,$2L$) as a function of L.

In Fig. 2.1 we show our raw QMC data of $L\rho_s$ at SU(10) for many different system sizes. The figure shows a very close zoom in to the VBS to magnetic transition, and the crossing points of system size pairs (L,$2L$) are plotted as the color points. We have ensured that all of our measurements are converged to the zero temperature limit by setting $\beta = 4L$ so that our scaling analysis is not muddled by finite temperature effects.

Now that we have extracted the values of the crossing points of $L\rho_s$ for different pairs of system sizes (L,$2L$), we can examine the scaling of both the x-coordinates of those points and the y-coordinates. We begin by handling the x-coordinates of the crossing points, corresponding to the estimates of the critical coupling, as the analysis

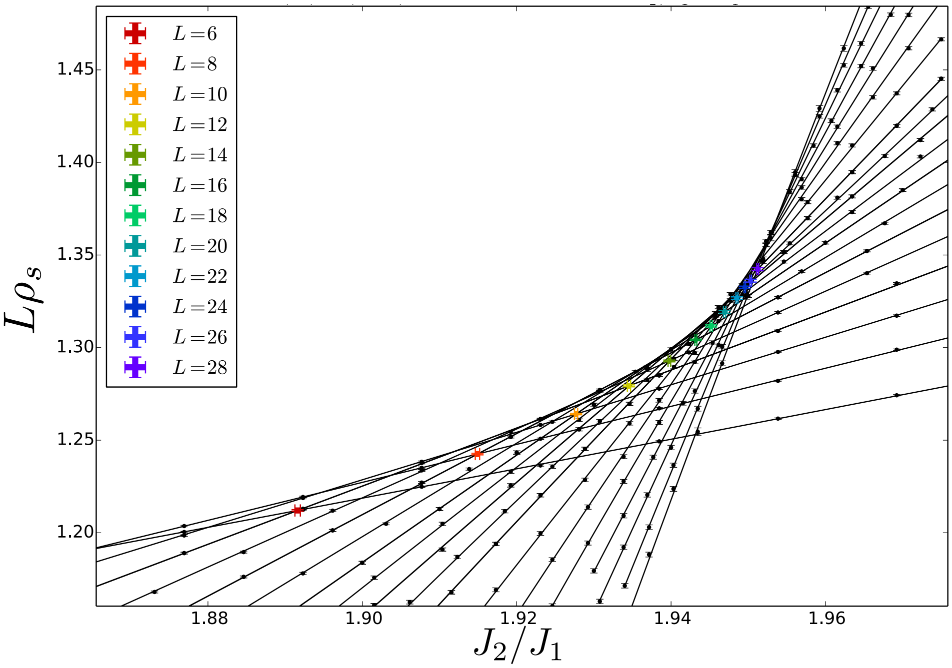

Figure 2.1: Here we show $L\rho_s$ as a function of J_2/J_1 for different system sizes (LxL) lattices for SU(10) zoomed in at the VBS to magnetic transition. The crossing points of pairs of system sizes (L,$2L$) are marked by the colored points. The black dots are the actual values of $L\rho_s$ obtained by QMC simulation, where the biggest system size used here is $L = 56$. The black lines are fits to 3rd order polynomials, which we use to interpolate our data in order to estimate the crossing points. Error bars on the crossing points are computed by bootstrapping our numerical data and performing many synthetic fits.To ensure that finite temperature effects do not play a role in the scaling of our $L\rho_s$ crossing points, we have set $\beta = 4L$, which we have ensured converges our measurements to the zero temperature limit. The crossing points that have been extracted here will be used for the rest of the analysis.

is slightly simpler there.

It is expected that the critical coupling, which we will refer to at g^*, should scale as $g^*(L_{\min}) = aL^\nu + b$ [2]. Here we take $\nu = -|\nu|$ to be negative, meaning that the critical coupling approaches a constant in the thermodynamic limit. Using this as our scaling form, in Fig 2.2 we show our numerical fit to the finite size critical coupling data and the associated fit parameters.

We have found the the critical coupling produces a very nice fit of our scaling form with just one power of L, and no use of sub-leading corrections (another term with a different power of L). We now analyze the scaling of $L\rho_s$ itself, as estimated from the

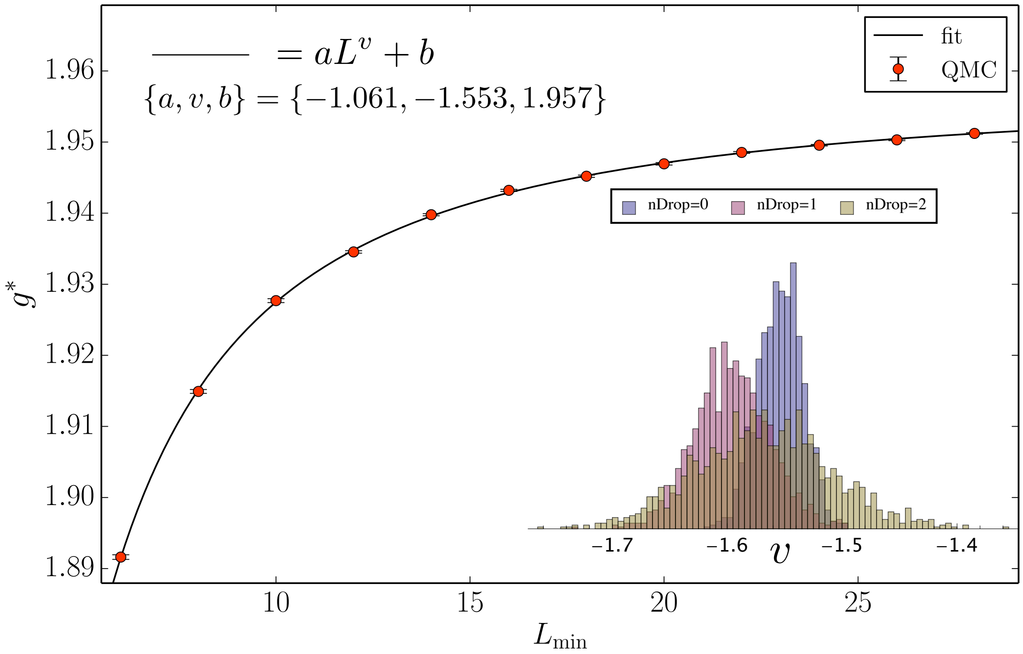

Figure 2.2: Here we perform numerical fits to the scaling form of the critical coupling values extracted from the crossing points of $L\rho_s$ shown in Fig. 2.1 for SU(10). The finite size scaling form for the the critical coupling g^* is shown in the upper left, and the fit values used to plot the black line are given just below the scaling form. We find excellent agreement between the scaling form and our numerical data. Furthermore, the fit parameters are relatively insensitive to which data points are included in the fit. This is shown in the bottom right, where our numerical data is bootstrapped and the fit performed many times, producing a histogram of values of the fit parameters. This procedure is done first by including all of our data points in the fit (nDrop=0), then excluding the smallest value of $L_{\min}$ (nDrop=1), then excluding the smallest two values (nDrop=2).

height of the crossing values. In Fig. 2.3 we fit the critical values of $L\rho_s$ to the scaling form $L^u(a+bL^w)$, which is capable of distinguishing between a constant saturation as a function of system size ($u = 0$ and $w < 0$), versus a sub-linear divergence ($0 < u < 1$ and $w < 0$). In this case as well, we find an excellent fit of our numerical data to the scaling form. The fit is also quite stable and relatively insensitive to the exclusion of small system size data (not shown here). Our data that we have used so far in this study is consistent with $u = 0$.

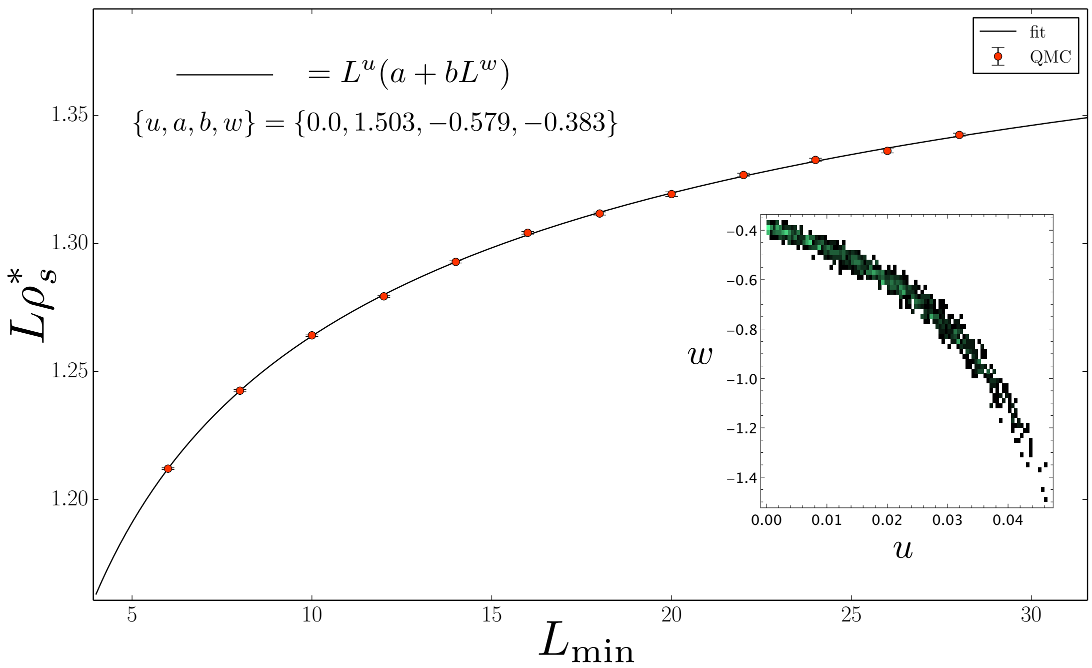

Figure 2.3: Here we fit the heights of the $L\rho_s$ crossing values as a function of L_{min} (the smaller system size used in the pair (L,$2L$)). We show the scaling form that has been used at the top left, which can distinguish between the case where $L\rho_s$ saturates to a constant versus if it diverges sub-linearly. The case when $L\rho_s$ saturates to a constant corresponds to when $u = 0$, which is in fact what we find here. The solid black line is plotted by setting $u = 0$ and using the optimal values of the other parameters, shown just beneath the scaling form. Again we produce histograms of the fit parameters by bootstrapping our data, which is shown in the lower right inset. Now that there are two important fit parameters (u,w), we show a histogram density plot, where dark green is low density and light green is high density. The histogram is produced by fitting to all of the data, although the results are similar even when excluding smaller system sizes in the fit.

2.5 Discussion

The result of our analysis on the critical values of $L\rho_s$, obtained by the crossing points, is that we find consistency with constant saturation as a function of system size (not sub-linear divergence, as in the SU(2) case). The picture so for seems convincing, despite the lack of larger system sizes and different values of N, however the objective is to pursue this with more computer time in the future. This result is quite interesting, suggesting a stark difference between the $N = 2$ case, and what happens at larger N.

The next important question in this work relates to how this picture evolves as $N \to 2$. As previously mentioned, we have access to the deconfined transition for all $N \geq 5$ with our particular model here. It is also possible, however, to add in a Q-interaction that favors VBS order. In this case we can start from a magnetically ordered state and tune toward the VBS using the Q-term. This will allow us to access the transition for $2 \leq N \leq 4$ [26]. It would be interesting to see how the scaling behaves for both $N = 3$ and $N = 4$. It is possible that an effectively enlarged symmetry in the $N = 2$ case is responsible for the anomalous scaling [28].

2.6 Conclusion and Outlook

In this chapter we have introduced an SU(N) symmetric spin Hamiltonian, which is the prototypical lattice model realizing deconfined criticality (including the J-Q models and the case $N = 2$). This model forms the foundation of the rest of the work to be carried out in this thesis. Additionally we have investigated a new feature of this model that has so far not been addressed.

We have been motivated here by the fact that deconfined criticality in the J-Q model at $N = 2$ exhibits anomalous critical scaling of various quantities including the spin stiffness. Here we have addressed the scaling of the spin stiffness at the transition for SU(10) and found, based on the limited system sizes available so far, that conventional critical scaling is recovered. Namely, the $L\rho_s$ saturates to a constant at the transition, validating the standard critical scaling.

We would clearly like to extend the scope of the present study. We would firstly like to include larger system sizes to ensure that our scaling behavior is not reflective of finite size effects. Secondly, and more interestingly, we would like to carry out an identical analysis at $N = 3$ and $N = 4$ in the SU(N) J-Q model, which will help us to determine if the $N = 2$ case is somehow special, and at what point conventional critical scaling appears.

Chapter 3 SO(N) Deformations and Spin Liquids

3.1 Introduction

Frustration in quantum magnetism has played a central role in the discovery of phases of matter without any classical analogue, most notably quantum spin liquid states [8]. These spin models are typically constructed from spin degrees of freedom that transform according to representations of the group SU(2), or SO(3) in the case of integer spin. Interest, however, has grown to include spin models with larger symmetry groups such as SP(N) [29] and SU(N) [1,22,30,31]. Originally introduced as a theoretical tool for solving models in the large-N limit [21], these models have become interesting in their own right due to the appearance of exotic phases as a function of N, and the ability to realize these models experimentally in ultra cold atom systems [32].

SO(N) spin models have also recently been explored in the context of quantum Monte Carlo [33], producing a surprisingly rich phase diagram consisting of valence bond solid states, magnetic states, and spin liquids. The study of SO(N) models are also motivated by the fact that they often describe systems that are composed of two or more order parameters that hybridize into a composite object [28,34].

In this work we will explore SO(N) spin models from the perspective of introducing anisotropy into the well studied SU(N) symmetric spin models [1] realizing deconfined criticality that we have investigated in the previous chapter. Along these lines, we will pursue a model that allows us to take the SU(N) symmetric model on the square lattice as a starting point. Then by increasing the strength of next-nearest-neighbor couplings, we reduce the symmetry to that of SO(N), while maintaining the square lattice symmetry important for deconfined criticality. We will first be interested in the fate of the deconfined critical point when anisotropy is added, then we will go on

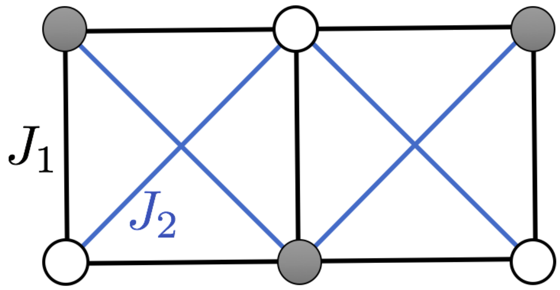

Figure 3.1: The lattice used for the study of our SO(N) symmetric Hamiltonian in Eqn. (3.1). J_1 bonds (black) connect nearest neighbors of the square lattice and J_2 bonds (blue) connect next-nearest neighbors. Here sites on one sublattice are in white and those on the other sublattice are black. Since the J_2 bonds couple sites on the same sublattice, the symmetry of the model becomes SO(N).

to explore the phase diagram as a whole.

3.2 Lattice Model

Here we introduce the Hamiltonian that will allow us to probe the effect of SO(N) anisotropy on SU(N) symmetric deconfined critical points. The Hamiltonian can very simply be written as a sum of two terms:

$$H_{\mathrm{SO}(N)} = -\frac{J_1}{N}\sum_{\langle ij\rangle} P_{ij} - \frac{J_2}{N}\sum_{\langle\langle ij\rangle\rangle} P_{ij}, \tag{3.1}$$

where $P_{ij} = \sum_{\alpha,\beta} |\alpha_i\alpha_j\rangle\langle\beta_i\beta_j|$ is the projection operator introduced in the previous chapter in the context of SU(N) deconfined criticality. The first sum in the Hamiltonian (J_1) is over nearest neighbors of a square lattice and the second sum is over next-nearest neighbors (J_2). This is depicted in Fig. 3.1.

Firstly, when $J_2 = 0$ in this model, we are of course left with the familiar SU(N) symmetric Hamiltonian that was discussed in the previous section. We know that there is Néel order for $N < 5$ and VBS order for $N \geq 5$. In between there is a continuous deconfined quantum critical point (continuous transition) that we have previously studied in great detail.

Here we are interested in the introduction of J_2, which couples together sites on the same sublattice. This in turn reduces the symmetry from SU(N) to SO(N). Importantly, however, the model maintains its square lattice symmetry, and near the $J_2 = 0$ axis the degenerate VBS ground states found in the SU(N) symmetric models are still present. Even as J_2 is increased, the simplicity of the lattice will enable us to easily detect different VBS ordering momenta, as will be presented in the following sections.

It is worth mentioning that if we take $J_1 = 0$ and J_2 finite, then our lattice becomes two independent square lattices, and again the physics is identical to the SU(N) symmetric case. We will be interested primarily with what becomes of the deconfined critical point when we turn on J_2, which amounts to addressing the fate of the SU(N) symmetric deconfined fixed point when SO(N) anisotropy is added.

3.3 Measurements

All of our observables will be based on Fourier transforms of correlation functions, which will be computed and averaged in the quantum Monte Carlo simulations. In order to detect magnetic order in this system, we will measure the the following spin-spin correlation function:

$$C_Q(i,j) = \frac{1}{N}\sum_{\alpha}\langle(|\alpha_i\rangle\langle\alpha_i| - 1/N)(|\alpha_j\rangle\langle\alpha_j| - 1/N)\rangle. \tag{3.2}$$

For three components, this expression is quartic in the spin-1 generators [35] (quadrupolar order). From a practical point of view, the interpretation of this correlator is quite simple, it checks for long range magnetic order corresponding to tiling the lattice with one color (analogous to a ferromagnet). The factor of $-1/N$ ensures that if we are in a magnetically disordered phase, then the correlator will go to zero at long distances.

This correlation function is diagonal in the spin basis, thus it can very simply be measured by looking at the state of the spins on any one time slice, usually the zeroth time slice for simplicity. Furthermore, in order to reduce the number of correlators that need to be stored, we make use of translational invariance to only store correlators at different separation differences, resulting in an $L_{\mathrm{x}} \times L_{\mathrm{y}}$ matrix.

The total squared "magnetization" (square of the quadrupolar order parameter) is given by the the Fourier transform of Eqn. (3.2) at zero momentum. The benefit of storing the entire correlation function as opposed to simply printing out its sum is that we can construct Fourier transforms at any momentum. The structure in momentum space near an ordering transition allows us to construct ratios of Fourier components that show a crossing point near the transition. For quadrupolar order, we construct the ratio as follows:

$$\mathcal{R}_Q = 1 - \tilde{C}_Q(2\pi/L, 0)/\tilde{C}_Q(0,0). \tag{3.3}$$

Here $\tilde{C}_Q(0, 2\pi/L)$ can equally well be used to construct the ratio, in fact any momentum not corresponding to a Bragg peak will work. The nearby momentum used here are chosen because they offer the best resolution in identifying the presence a Bragg peak.

In order to characterize VBS order, we measure bond-bond correlation functions in our QMC simulations. These are defined as follows:

$$C^{\hat{a},\hat{b}}_{\mathrm{VBS}}(\vec{r}) = \langle |s^{\hat{a}}_0\rangle\langle s^{\hat{a}}_0||s^{\hat{b}}_{\vec{r}}\rangle\langle s^{\hat{b}}_{\vec{r}}|\rangle. \tag{3.4}$$

This is a correlation function of SO(N) singlet projectors. Here we have defined the two-site SO(N) singlet as

$$|s^{\hat{a}}_{\vec{r}}\rangle \equiv \frac{1}{\sqrt{N}} \sum_{\alpha} |\alpha_{\vec{r}}\alpha_{\vec{r}+\hat{a}}\rangle \tag{3.5}$$

where $\alpha_{\vec{r}}$ is a spin at spatial location $\vec{r}$, given by its (x,y) coordinates, and $\alpha_{\vec{r}+\hat{a}}$ is either a nearest neighbor or next nearest neighbor along one of the bond directions (denoted by $\hat{a}$). $\hat{a}$ for this model can be (1,0), (0,1), (1,1), (-1,1). The“hat” here is just a notational scheme and should not be interpreted as unit magnitude.

As the possible VBS states in the phase diagram in this model are not known, we store the bond-bond correlation functions with every possible combination of bonds, both with equal orientations of the bonds and unequal orientations. As such, we can already anticipate the various ordering momenta associated with correlators of particular orientations. For instance, when $J_2/J_1 \ll 1$ we anticipate columnar VBS order for $C_{\text{VBS}}^{(1,0),(1,0)}(\vec{r})$ and $C_{\text{VBS}}^{(0,1),(0,1)}(\vec{r})$. The former case is depicted in Fig. (1.1), where the diagonal bonds are not drawn. The ordering momentum in this case is (π,0), which allows us to construct the crossing ratio

$$\mathcal{R}_{\text{VBS}} = 1 - \tilde{C}_{\text{VBS}}^{(1,0),(1,0)}(\pi + 2\pi/L, 0)/\tilde{C}_{\text{VBS}}^{(1,0),(1,0)}(\pi, 0). \tag{3.6}$$

A very similar ratio can be constructed for the y-oriented bonds, except with ordering momentum (0,π), and in practice these are averaged over in the QMC to improve statistics. In Fig. (3.2) we show some example structure factors (Fourier transforms) of the VBS correlation functions. Here Bragg peaks clearly emerge in the limits that we expect, namely when the diagonal bonds are weak where we see columnar VBS order on the x and y oriented bonds, and also when the diagonal bonds are strong where we see columnar VBS order tilted at 45 degrees on the diagonal bonds. The data that we will present in the following sections will focus on these two particular types of orders and how they behave as we tune the anisotropy (J_2/J_1).

3.4 Numerical Results

We would like to sketch out the phase diagram of this model as a function of N and J_2/J_1, and along the way uncover the nature of the phase transitions that take place. We will firstly be interested with what happens near the “square lattice axis” (J_2/J_1 is small). This is of particular interest due to the fact that there is a deconfined

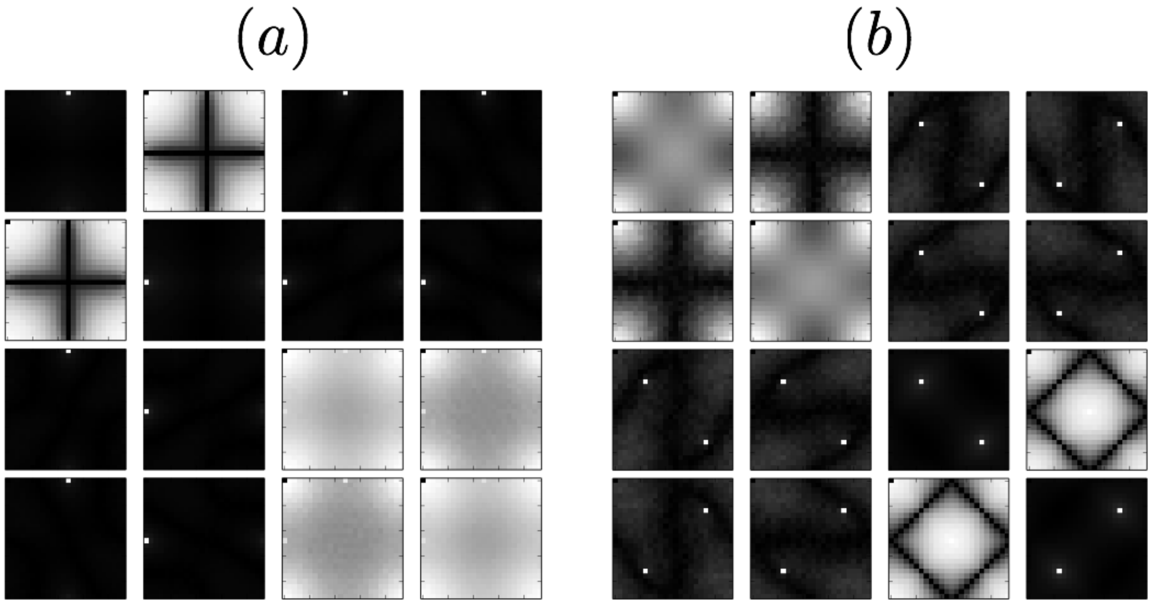

Figure 3.2: Here we show the Fourier transform of the various VBS correlation functions of a SO(7) $L = 24$ system for $J_2/J_1 = 0.14$ (panel a) and $J_2/J_1 = 7.0$ (panel b). All of the panels display every combination of $\hat{a}$ and $\hat{b}$ in Eqn. (3.4), such that $\hat{a}$ labels the rows in the order (1,0),(0,1),(1,1),(1,-1) and $\hat{b}$ labels the columns in the same order. The coordinates in each individual panel are the x and y momenta (q_{x}, q_{y}), and the origin is located at the upper left corner. Panel (a) represents the limit when J_2 is very weak, and we essentially have a square lattice. At this value of N on the square lattice, columnar VBS order prevails, which can clearly be seen by the Bragg peaks appearing at (π,0) and (0,π) in $\tilde{C}_{\mathrm{VBS}}^{(1,0),(1,0)}(\vec{q})$ and $\tilde{C}_{\mathrm{VBS}}^{(0,1),(0,1)}(\vec{q})$, respectively. Panel b illustrates the opposite limit, where the x and y bonds are very weak, and the lattice can be though of as two independent square lattices, each tilted at 45 degrees. Columnar VBS order appears in this case as well, except on the diagonally oriented bonds. This again can be seen in the Bragg peaks occurring in $\tilde{C}_{\mathrm{VBS}}^{(1,1),(1,1)}(\vec{q})$ and $\tilde{C}_{\mathrm{VBS}}^{(1,-1),(1,-1)}(\vec{q})$, which are the last two panels along the diagonal.

critical point located on the J_2/J_1 axis between $N = 4$ and $N = 5$ [21]. If we are near this critical point, we can ask what is the effect of adding anisotropy, corresponding to a small but finite J_2/J_1. Thinking in terms of renormalization group ideas, there are several possible scenarios: firstly, the anisotropy could be irrelevant, meaning that the same critical point would extend to finite values of J_2/J_1, appearing as a line in the phase diagram. Secondly, the anisotropy could be a relevant perturbation to the deconfined fixed point. In this case there could be another fixed point in a different universality class that would describe the criticality at finite anisotropy,

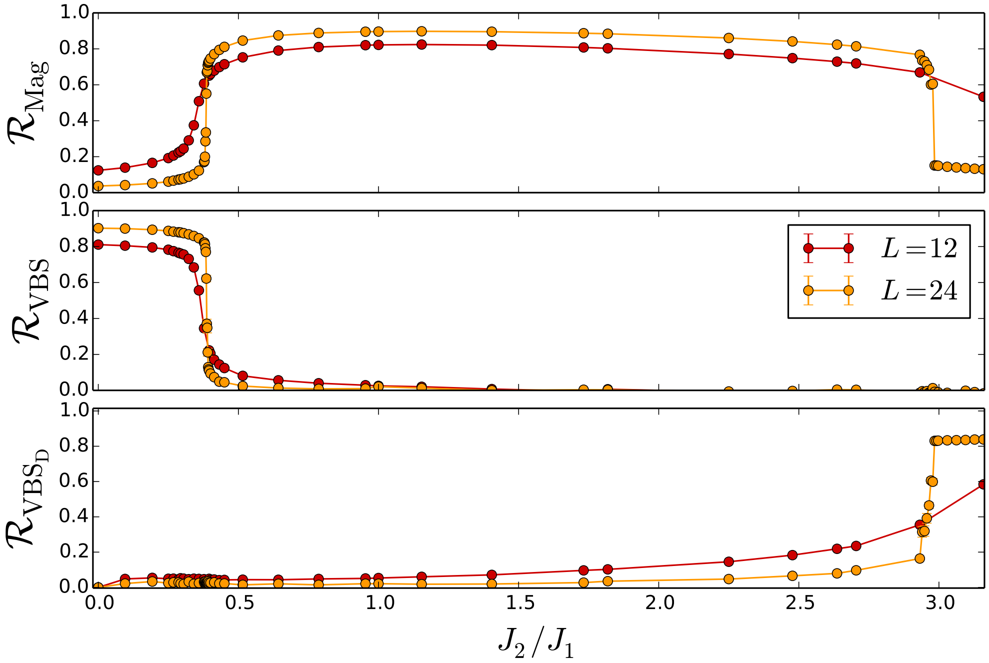

Figure 3.3: Here we show a cut through the phase diagram of an SO(7) system as a function of anisotropy J_2/J_1. Using two system sizes and plotting the ratios allow us to estimate the location of phase transitions, given by the crossing points. The top panel shows the magnetic ratio and the middle and bottom panels are the VBS and diagonal VBS ratios, respectively. As we expect, columnar VBS order is present for small values of J_2/J_1, as shown in the middle panel. VBS order transitions directly to magnetic order near $J_2/J_1 \approx 0.4$, as indicated by a VBS crossing (middle panel) and magnetic crossing (top panel) that occur approximately at the same value of the coupling. The story is similar near $J_2/J_1 \approx 3.0$, except there magnetic order gives way to columnar VBS order on the diagonal bonds.

or the perturbation could cause a flow to strong coupling, meaning no stable finite coupling fixed point and resulting in a first-order transition at finite anisotropy.

In order to address this question, we fix $N = 7$ and vary the anisotropy across the columnar VBS, magnetic, and diagonal columnar VBS phases. This is given in Fig. 3.3, where we show the ratios constructed from the three order parameters. The phase transitions along this cut are estimated based on the crossing points of the ratios for the two different system sizes. We conclude that for $N = 7$ there is a direct transition from the VBS phase to the magnetic phase at around $J_2/J_1 \approx 0.4$. Similarly at higher values of the coupling ($J_2/J_1 \approx 3.0$) there is another direct transition from magnetic

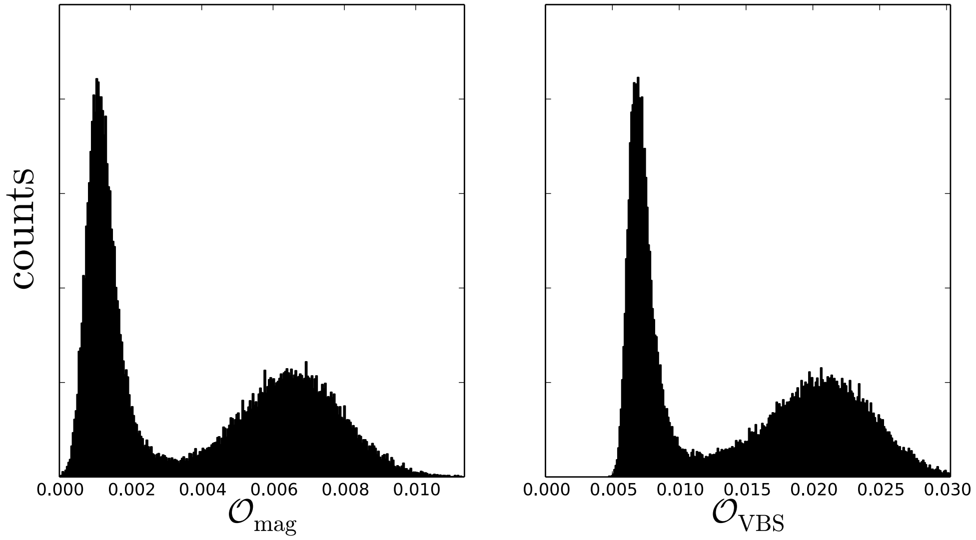

Figure 3.4: Histograms of the magnetic and columnar VBS order parameters near the transition at $J_2/J_1 = 0.385$ on an $L = 24$ SO(7) system. In order to generate the histograms, we measure many bins with very few Monte Carlo sweeps per bin, which produces a time series of our measurements. The time series for our measurements shows a clear switching behavior between two distinct values that is illustrated by a double peaked histograms. Double peaked histograms are a smoking gun signal of first-order behavior, where the free energy has two local minima that cross as a function of the coupling.

to VBS on the diagonal bonds.

In order to investigate the nature of the phase transition, we collect data very close to the VBS-magnetic transition at $J_2/J_1 = 0.385$ on an $L = 24$ SO(7) system and produce histograms of the VBS and magnetic order parameters, as shown in Fig. 3.4. The fact that our Monte Carlo simulations display a switching between magnetic and VBS ordered configurations means that histograms of the order parameters show a double peaked structure. This is indicative of a first-order phase transition, where the free energy contains two local minima in the landscape of configurations. As the coupling is varied, the global minima jumps from one local minima to the other, producing a discontinuity in the values of the order parameters at the transition in the thermodynamic limit.

In light of our histogram data at $N = 7$, we conclude that $\mathbb{CP}^{N-1}$ fixed point that

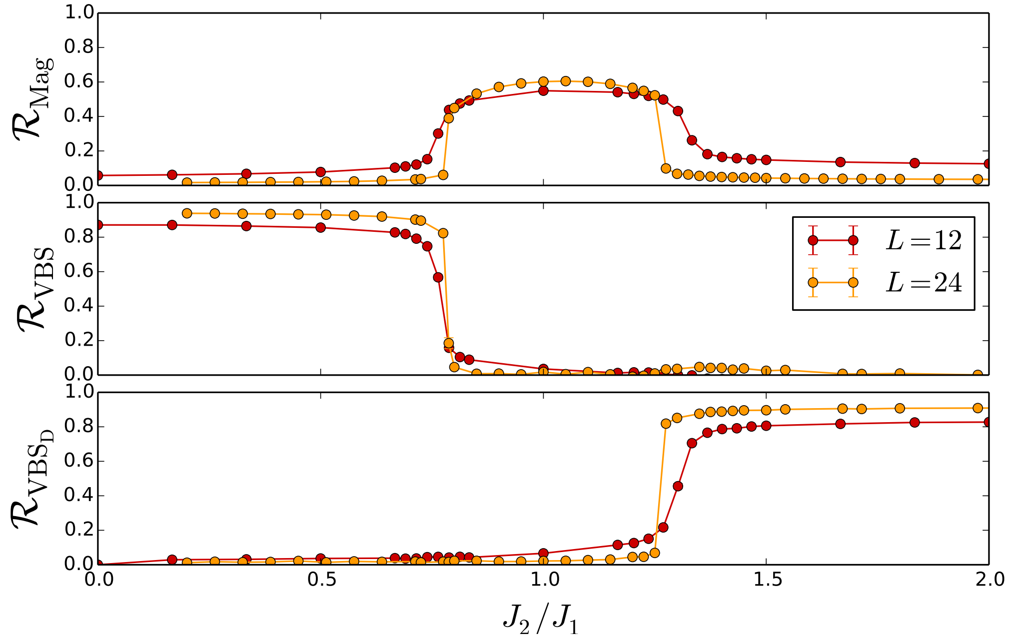

Figure 3.5: Here we show the ratios at $N = 12$, where we find similar behavior as in Fig. 3.3. It is clear that at these larger values of N, the intermediate magnetic phase occupies a much smaller region of the phase diagram. Interestingly, it appears as if the phase boundaries become symmetric about $J_2/J_1 = 1$ as N is made large.

describes continuous magnetic to VBS phase transitions in SU(N) symmetric models is unstable to the presence of SO(N) anisotropy. This is manifested in our lattice model as a first-order transition between VBS and magnetic phases when anisotropy is added.

Having addressed the question of deconfined criticality in the presence of SO(N) anisotropy, we go on to fully explore the phase diagram of our model as a function of N and J_2/J_1. Given that previous work on the triangular lattice revealed a spin liquid at large values of N [33], another important question concerns at which value of N the VBS to magnetic transition splits apart, revealing an intermediate spin liquid phase.

Moving to $N = 12$ we show the ratios as a function of anisotropy in Fig. 3.5. Here we find as similar story as in Fig. 3.3, except it becomes clear that at larger values of N, the magnetic phase occupies a much smaller region of the phase diagram. It is

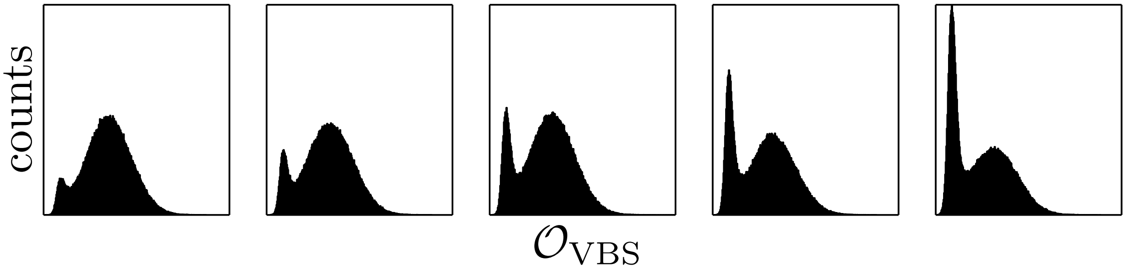

Figure 3.6: Here we show the histogram of the VBS order parameter ($\mathcal{O}_{\text{VBS}}$), for an L=24 system across the VBS to magnetic transition. Here each panel is taken at a different value of J_2/J_1, where from left to right the values are (0.78, 0.78057, 0.78114, 0.78171, 0.78229). Again we clearly see double peaked behavior across the transition, indicative of a first-order transition. We have not plotted the histograms of $\mathcal{O}_{\text{mag}}$ as they show no signs of double peaks for these values of the coupling. This is likely due to the fact that a spin liquid phase has begun to emerge in the intermediate region between VBS and magnetic phases, which will become more obvious at $N = 13$.

also interesting to note that the phase boundaries become roughly symmetric about $J_2/J_1 = 1$.

Again we examine the behavior near the VBS to magnetic transition at $N = 12$ to determine whether or not it is still first order in nature. In Fig. 3.6 we show histograms of the VBS order parameter $\mathcal{O}_{\text{VBS}}$ for different values of the coupling across the VBS to magnetic transition. Again we clearly see a double peaked structure across the transition, indicative of first-order behavior. Here we have not plotted histograms of the magnetic order parameter, since it shows no signs of double peaks for these values of the couplings. This we attribute to the presence of a spin liquid phase that begins to emerge between the VBS and magnetic phases, which will become more clear at $N = 13$.

We next move to $N = 13$, where we first see clear evidence that the VBS to magnetic transition splits, revealing a featureless intermediate phase, the spin liquid. Fig. 3.7 shows a zoom in of the VBS crossing for $J_2/J_1 < 1$, which shows very little drift as a function of system size. The important feature here is that the magnetic crossing, which is not visible in the plot, does not appear in the vicinity of the VBS crossing. This indicates that the VBS phase does not transition directly into

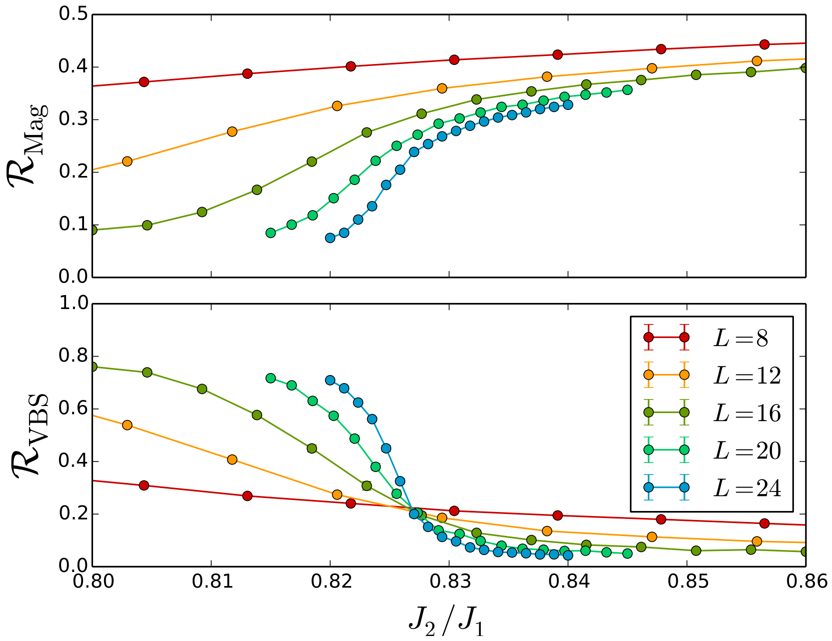

Figure 3.7: Here we focus in on the VBS ratio crossing at $J_2/J_1 < 1$ for $N = 13$. We see a very clean crossing of the VBS ratio around $J_2/J_1 \approx 0.8275$ with little drift as a function of system size. Most importantly, we see no crossing of the magnetic ratio on the domain of this plot, indicating that the VBS is transitioning directly to the disordered spin liquid phase.

the magnetic phase, but rather it transitions into an intermediate spin liquid phase which breaks no symmetries.

Again we look at the histograms of the VBS order parameter for the case $N = 13$ (Fig. 3.8) on an $L = 24$ system across the transition. Here we can see a qualitative change taking place in the appearance of the histograms, which were collected with similar parameters as $N = 12$ where the double peaks were clearly pronounced. For $N = 13$ we begin to see the two peaks in the histograms merging together. This is evidence that the first-order transition is weakening to a continuous one, suggesting that the VBS to spin liquid phase transition in continuous in nature. This conclusion is further supported by the fact that the VBS ratio produces an clean crossing with minimal drift as a function of system size.

If the VBS to magnetic transition has truly split, giving rise to an intermediate

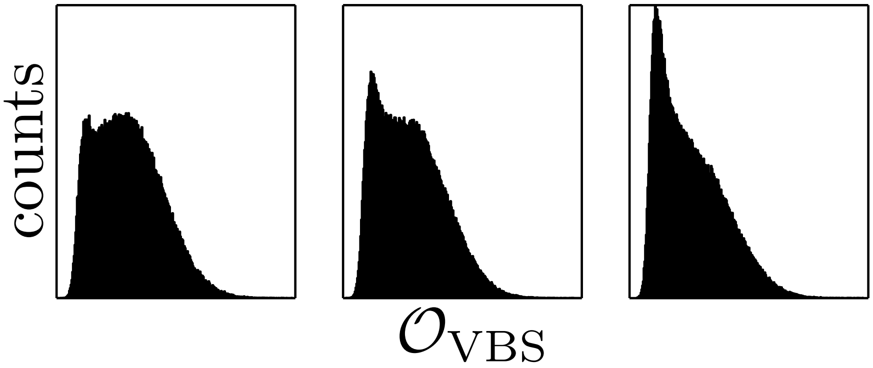

Figure 3.8: Histograms of the VBS order parameter ($\mathcal{O}_{\mathrm{VBS}}$) across the VBS to spin liquid transition for $N = 13$, $L = 24$ and J_2/J_1=(0.8198, 0.82014, 0.82082) (left to right). Here we notice a clear qualitative change in the appearance of the VBS histograms as compared with the $N = 12$ case. Here the double peaks, which signal first-order behavior, have begun to merge together indicating that the first-order transition is weakening and becoming continuous. This feature, when combined with the clean crossing point of the VBS ratio (Fig. 3.7), provides strong evidence that the VBS to spin liquid transition is continuous.

spin liquid phase, the question remains if the magnetic phase is still present in the phase diagram at $N = 13$. To address this question we study the crossings of the magnetic ratio in order to estimate the location of the spin liquid to magnetic transition in the thermodynamic limit, this is shown in Fig. 3.9. Here, in stark contrast to the VBS ratio, we find significant drift of the magnetic ratio crossing. Therefore, in order to properly estimate the location of the spin liquid to magnetic transition, we must systematically study the crossing points of system sizes L and $2L$ as a function of L, which is plotted in the inset of Fig. 3.9. By plotting the crossing values as a function of $1/L$, we can estimate the location of the transition in the thermodynamic limit, which is given by the y-intercept. We have also plotted the location of the VBS transition, which we have simply estimated based on the location of the VBS crossing assuming negligible drift. Extrapolating finite sized data is difficult and dangerous, unless one is confident about the exact scaling form that is expected. Therefore we have contented ourselves here with an extrapolation "by eye," which indicates that the presence of an intervening phase (between the VBS and magnetic transitions)

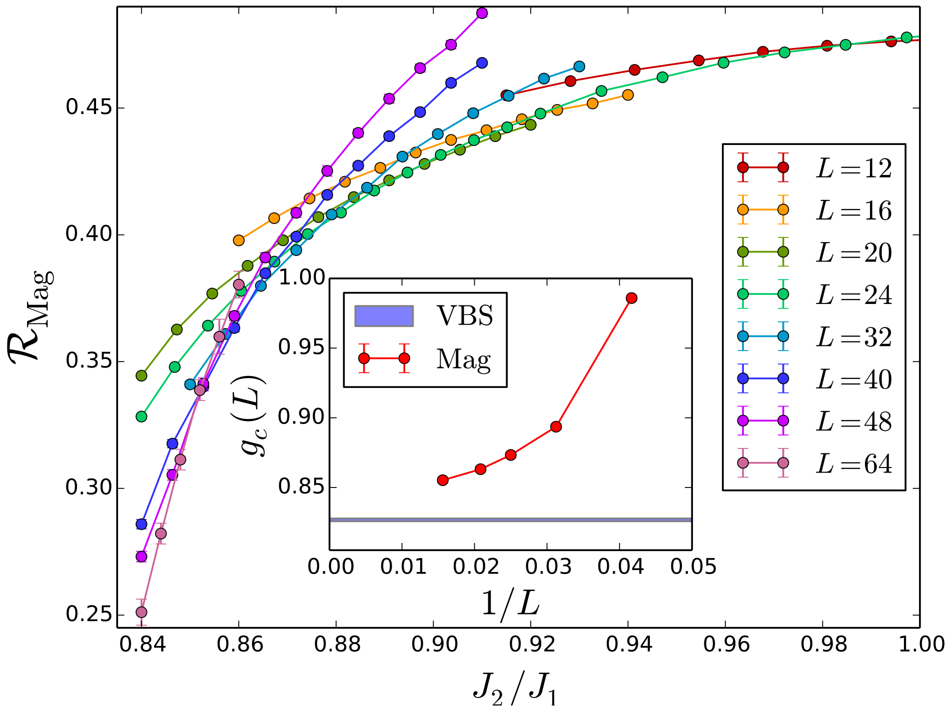

Figure 3.9: Here we show the crossing of the magnetic ratios at $N = 13$ for different system sizes. Unlike the VBS ratio crossings, the magnetic crossings show substantial drift as a function of system size. In order for us to properly estimate the location of the spin liquid to magnetic transition we must systematically study the crossing points of L and $2L$ as a function of system size (shown in the inset). Also plotted in the inset is the crossing point of the VBS ratio assuming a negligible drift there. Extrapolating to the y-axis gives the location of the transition in the thermodynamic limit. Without larger system sizes or performing potentially unreliable extrapolations, we see that an intermediate spin liquid phase likely intervenes between the VBS and magnetic phases.

seems reasonable.

In order to address what happens at larger values of N, it is most efficient to set $J_2/J_1 = 1$ and study the ratios as a function of N. In Fig. 3.10 we show the magnetic ratio as a function of $10 \le N \le 19$ for different system size. Here it is clear that the magnetic order dies completely at $N = 15$ and is most likely already gone at $N = 14$. Here we do not show the VBS ratios, although we have studied them for large N. The story there indicates the complete absence of VBS order at least up to $N \approx 19$. We however very quickly encounter ergodicity problems of our VBS measurements at

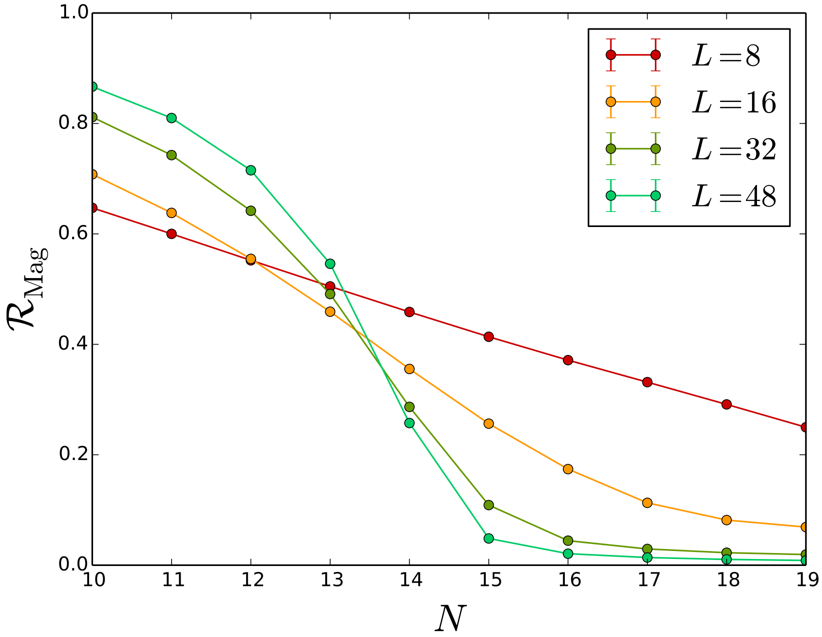

Figure 3.10: Here we show the magnetic ratio as function of N with $J_2/J_1 = 1$ fixed. We see that magnetic order clearly dies by $N = 15$ and is most likely already gone at $N = 14$. Here we do not show the VBS ratios, as we quickly encounter ergodicity issues of our VBS measurements at large N, resulting in a jittery signal that begins to turn on around $N = 19$. The result is that the spin liquid phase appears over an extended range of N along the $J_2/J_1 = 1$ axis, with a minimal extent of $15 \leq N \leq 18$.

large N, making it difficult to estimate the location of the transition. Regardless of this complication, it is clear that the spin liquid is extended over many values of N.

Based on the numerical results that we have so far presented, we can begin to sketch out a phase diagram for this model as a function of N and J_2/J_1, this is given in Fig. 3.11. In the discussion section we go on to discuss the interesting features of the phase diagram.

3.5 Discussion

We would now like to discuss the salient aspects of the model that we present in this section. A key feature of the this model is that it allows us to deform an SU(N) symmetric model into an SO(N) symmetric one, while preserving the symmetry of

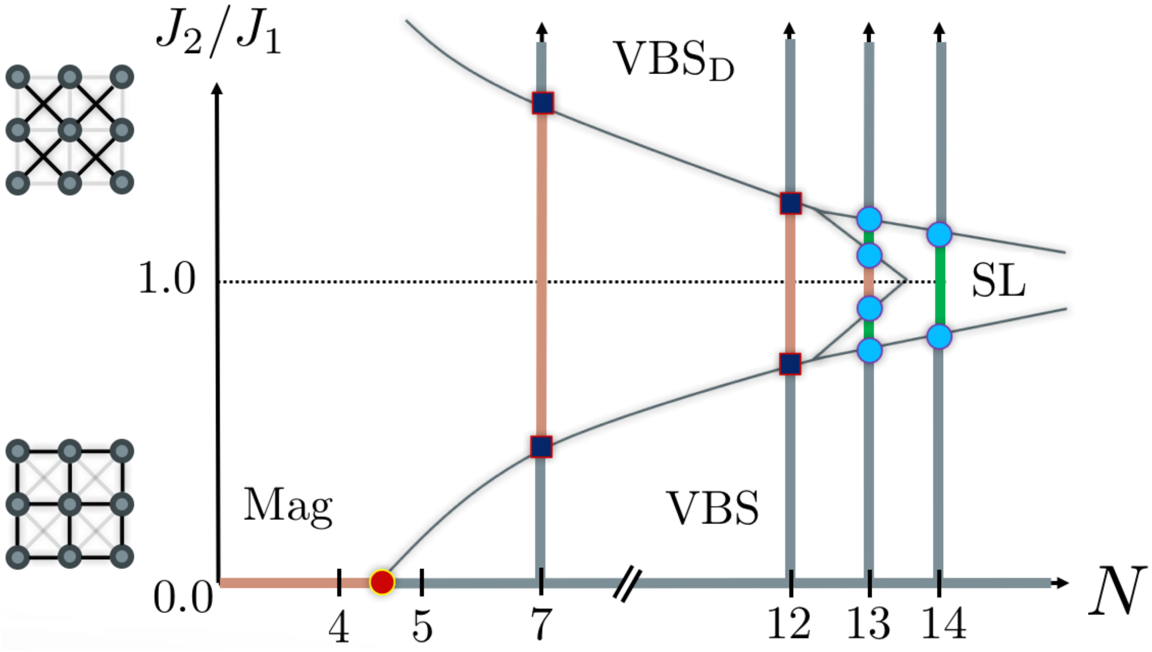

Figure 3.11: A cartoon of the phase diagram based on the numerical results that we have presented so far. Here the pink lines represent magnetic order (Mag) that we have measured in QMC and gray lines represent either VBS order on the vertical and horizontal bonds (VBS) or VBS order on the diagonal bonds (VBS$_\mathrm{D}$). The spin liquid phase (SL) is represented as green lines. The red circle on the $J_2/J_1 = 0$ axis represents the deconfined magnetic to VBS phase transition that is known to exist in the SU(N) symmetric models [1].The dark blue squares between phases represent first order phase transitions, where we see always first order transitions between VBS and magnetic phases. The light blue circles represent continuous transitions, which appear at the boundaries of the spin liquid phase. Here we have not drawn the phase diagram past $N = 14$, as our VBS data becomes unreliable at such large values of N. We believe however that the spin liquid phase extends at least up to $N = 18$, cutting out a large swath of the phase diagram. For illustrative purposes, on the left we have given a cartoon picture of the relative bond strengths on the lattice for small (bottom) and large (top) values of J_2/J_1.

the square lattice. Our first finding is that when SO(N) anisotropy is introduced, the VBS to magnetic transition shows clear signatures of first-order behavior. The interpretation of this result is that the deconfined $\mathbb{CP}^{N-1}$ fixed point that describes the magnetic to VBS transitions in the SU(N) symmetric models [16] is unstable to the presence of SO(N) anisotropy. Interestingly, this is contrary to a prediction made in a previous theoretical treatment [36].

Another interesting feature of this model, one that becomes apparent as N becomes larger, is the approximate symmetry about the $J_2/J_1 = 1$ axis. It is quite remarkable if this truly indicates the fact that the physics is identical both above and below that axis. If this is indeed the case, it is not at all obvious. Although for $J_2/J_1 \gg 1$ we have essentially decoupled square lattices, for values just slightly greater than 1 they are still strongly coupled, and yet a symmetry about $J_2/J_1 = 1$ would imply that the behavior is approximately the same as if only one square lattice is present. At this point a full analysis of the transition to the $\mathrm{VBS_D}$ phase is lacking, though it will be interesting to compare this to the VBS transition to verify if they are indeed the same.

A puzzling aspect of the data at $N = 12$, which we hinted at in the previous section, is the fact that the VBS order parameter shows a double peaked histogram across the VBS to magnetic transition, while the magnetic histogram remains smooth. We have attributed this the the possibility of a very thin intervening spin liquid phase, however it is quite clear that the VBS to spin liquid transition is continuous at larger N. A resolution to this apparent contradiction could come at larger system sizes, where it is possible that the two peaks in the VBS histogram will merge together, producing something similar to what is seen in Fig. 3.8. This would be the case if there truly were a very thin intervening spin liquid phase. Alternatively, it could be that the magnetic order parameter shows double peaked histograms at some slightly separated values of J_2/J_1. By going to larger system sizes, the points where the VBS and magnetic order parameters are double peaked could merge together, implying a direct first-order transition between VBS and magnetic phases. This detail goes beyond the purpose of our work here, which is to broadly explore the phase diagram of this model as a whole.

The most interesting aspect of the phase diagram is of course the spin liquid phase. The first thing to notice about this phase is that it persists through several values of N, in contrast to the same model on the triangular lattice where the model only shows spin liquid behavior at $N = 11$ (in the case of the triangular lattice nearest neighbor model) [33]. So far we have only asserted that VBS order is absent on the $J_2/J_1 = 1$ line at most for $N < 19$, although in order to clearly uncover the behavior in this limit, more careful numerical simulations are needed. It is indeed possible that the physics at large N is quite different from the triangular lattice case, where VBS order is very clearly observed at larger N, with no apparent ergodicity issues.

3.6 Conclusion and Outlook

In conclusion of this chapter, we have considered the effect of SO(N) anisotropy on deconfined critical points that exist between magnetic and VBS phases in SU(N) magnets. The result is a first-order transition when anisotropy is added. We then went on to explore the phase diagram of the SO(N) model as a whole, which exhibits an extended spin liquid phase that persists for many values of N. We found evidence that phase transitions into the spin liquid are continuous in nature, which supports the findings in [33].

More data still needs to be collected for this model in order to address some particular questions that still remain. We would like to know, for instance, the universality class of the critical point separating the VBS and spin liquid phases. It is believed that this will be in the same universality class as the 3D XY transition [37], though ultimately we would like to extract critical exponents from scaling collapses in order to verify this explicitly. It would be most suitable to carry out the collapses at $N = 14$, where the complication of a nearby spin liquid to magnetic transition is not present. The magnetic to spin liquid transition will most likely not be pursued, as the drift of the magnetic crossing point would indicate substantial corrections to critical scaling, complicating the analysis and forcing us to go to very large lattices.

Perhaps the biggest looming question in this model, and related models, is the nature of the spin liquid state. So far it has only been postulated that this phase is indeed a quantum disordered phase of matter, which preserves all symmetries and hence cannot be detected by any local order parameter [8]. Indeed, one of the best ways of uncovering the signatures of a spin liquid phase is with a nonlocal probe: the so-called "topological entanglement entropy" [38, 39]. We have so far pursued this direction, though we will not detail it in this dissertation. Our preliminary results indicate that indeed we have correctly identified this disordered phase and being a quantum spin liquid, which is characterized by long-range entanglement. The presence of this exotic phase in these simple quantum models opens up the possibility of investigating different spin liquid phases on other lattices and in three dimensions.

Chapter 4 First-Order Superfluid to VBS Transitions at Small N

The following chapter has been take from Ref. [40].

4.1 Introduction

Quantum phase transitions have emerged as an important paradigm in the study of quantum many-body phenomena. [9] Deconfined criticality is a novel field theoretic proposal for a continuous transition between a magnet or superfluid that breaks an internal symmetry and a valence bond solid that breaks a lattice translational symmetry. [16, 17] The field theories realized at these new critical points are strongly coupled gauge theories, which are rather fundamental and hence connected to a wide range of problems, [3,41] making the study of deconfined criticality of general interest in theoretical physics. The study of deconfined critical points has been significantly enhanced by the availability of sign problem free quantum Monte Carlo (QMC) simulations which are able to access the strong coupling physics of the emergent gauge theories in some particular Marshall positive Hamiltonians that host this phase transition. [1]

Historically, in the discovery of deconfined criticality, a prominent role was played by the "easy-plane" deconfined critical point, which is most naturally realized in lattice models of superfluids. The square lattice quantum XY model has been studied extensively in the last few decades as the simplest quantum lattice spin model for a superfluid. The model can be written in the following ways,

$$\begin{aligned} H_{XY} &= -J\sum_{\langle ij\rangle}\left(S_i^x S_j^x + S_i^y S_j^y\right) && (4.1) \\ &= -\frac{J}{2}\sum_{\langle ij\rangle}\left(S_i^+ S_j^- + S_i^- S_j^+\right), && (4.2) \end{aligned}$$

where the $\vec{S}_i$ are the usual $S = 1/2$ Pauli matrices on site i. The model has only a sub-group of the SU(2) symmetry of the Heisenberg model: it has a $U(1)$ rotation symmetry about the $\hat{z}$ axis and a Z_2 symmetry of flipping the S^z components. We note here that the sign of J is inconsequential, since it can be changed by a unitary transformation. The model H_{XY} is Marshall positive and hence free of the sign problem of quantum Monte Carlo. Exploiting this fact, extensive numerical simulations have shown that H_{XY} has long range superfluid order at $T = 0$. To study the destruction of superfluid order in the ground state, a sign-free generalization of the quantum XY model to include a four spin coupling K was introduced, [42]

$$H_K = -K \sum_{\langle ijkl \rangle} \left(S_i^+ S_j^- S_k^+ S_l^- + S_i^- S_j^+ S_k^- S_l^+ \right) \tag{4.3}$$

It has been shown that this model hosts three phases, a superfluid state at small K/J, valence-bond solid order for K/J and checkerboard order for large K/J. The phase transition between VBS and checkerboard was found (as expected) to be strongly first order. On the other hand the fate of the transition between superfluid and VBS in this model has remained enigmatic, while no evidence for a discontinuity have been observed in this model, large scaling violations may not be interpreted consistently as a continuos transition. [43] This transition if continuous would have been the first example of a "deconfined critical point," its first numerical study even predating the field theoretic proposal. The square lattice easy-plane deconfined critical point played a prominent role in the original proposal and additionally it has been shown that should the superfluid-VBS transition in the quantum XY model be continuous, it would be a rare example of a self-dual critical point, [44] which can be connected to various interesting field theoretic formulations with topological terms. [45] We note here that some direct studies of the effective field theory [46, 47] and other quantum models on frustrated lattices [48, 49] which are believed to be in the same universality class have found evidence for a first order transition. In the meantime, attention in deconfined criticality has shifted to the study of the fully SU(N) symmetric Hamiltonians, [10, 21, 50] which have shown compelling evidence for a continuous transition.

However, given the important role that the square lattice XY model has had as the first putative host of deconfined criticality, it remains of interest to have an unambiguous answer to the nature of the superfluid-VBS transition in this model. Instead of addressing this issue in the J-K model, where the results of the simulations are hard to interpret [43] we study a different model which can be understood as an easy-plane generalization of the SU(2) symmetric J-Q model. [10] We provide clear evidence that the transition in this model is direct and discontinuous both for superfluid and the VBS order. Additionally, we are able to provide a simple way to generalize the easy-plane J-Q model to larger-N. Through large scale numerical simulations we show that $H^N_{J_\perp Q_\perp}$ hosts the superfluid-VBS phase transition for all $N \leq 5$. We provide evidence that this transition remains first order for $N = 5$, which leads us to conclude that easy-plane deconfined criticality is generically first order for small-N.

The chapter is organized as follows. In Sec. 4.2, we introduce the new easy-plane J-Q model, $H^N_{J_\perp Q_\perp}$ and write it down in different ways, emphasizing how it is connected to previously studied models. In Sec. 4.3 we show how it maps to a particular family of loop models in one higher dimension and use this representation to formulate an efficient Monte Carlo algorithm. In Sec. 4.4 we discribe our measurments, and in Sec. 4.5 we discribe the properties of our model with $Q = 0$. In Sec. 4.6, we present results of simulations of $H^N_{J_\perp Q_\perp}$ on the square lattice, focussing on the first-order nature of the phase transitions in this model. Finally, in Sec. 4.7, we provide our conclusions and outlook.

4.2 Lattice Hamiltonian

It is useful to write our Hamiltonian in a few different ways to elucidate certain diverse aspects. First let us consider the generalization of the XY model in the form, Eq. (4.1) to arbitrary-N. A natural way to do this on a bipartite lattice in the spirit of the work of Affleck, [22] is to consider the following Hamiltonian,

$$H_{J_\perp}^N = -\frac{J_\perp}{N} \sum_{\langle ij \rangle} \sum_{a \in od} T_i^a T_j^{a*}, \tag{4.4}$$

where the T_i are $N \times N$ matrices acting on site i, which are the generators of SU(N). Here we choose the normalization such that $\mathrm{Tr}[T^a T^b] = \delta_{ab}$. These generators act on a local Hilbert space which now can take N different colors and are denoted by $|\alpha\rangle_i$. We note that i is always chosen on the A sub-lattice and j is chosen on the B sub-lattice, so that spins on one sublattice transform in the fundamental and spins on the other sublattice transform under the conjugate to fundamental representations. The important difference with the usual fully SU(N) symmetric Heisenberg model is the sum on generators a, is restricted to the off-diagonal generators. It is well known that of the $N^2 - 1$ generators of SU(N), $N - 1$ are diagonal and $N^2 - N$ are off-diagonal. The restriction of the sum to the $N^2 - N$ off diagonal generators guarantees that when $N = 2$, we recover the usual XY model. For larger N, Eq. (4.4) is a convenient large N generalization of the XY model. We note here that the restriction to off-diagonal genertors reduces the symmetry from SU(N) to a $\mathrm{U}(1)^{N-1} \times \mathrm{S}_N$ subgroup (where S_N is the permutation group), which generalizes the $\mathrm{U}(1) \times \mathrm{Z}_2$ of Eq. (4.1). Physically this corresponds to rotations about the directions of the $N - 1$ diagonal generators and a discrete relabeling of the colors. We shall call this symmetry ep-SU(N) symmetry. Just like in the fully symmetric SU(N) case, the virtue of staggering the representation is that an A-B pair can form an ep-SU(N) singlet for all N. For sites $i \in A$ and $j \in B$, the singlet may be written as $|s_{ij}\rangle = \frac{1}{\sqrt{N}} \sum_{\alpha=1}^{N} |\alpha_i \alpha_j\rangle$

Having written the model formally in terms of the SU(N) generators helps us see that model is a large-N extension of H_{XY}. To get a better intuition for the matrix elements of the model we now write it directly in terms of the local Hilbert space. In terms of which, Eq. (4.4) takes the simple form,

$$\begin{aligned} H^N_{J_\perp} &= -\frac{J_\perp}{N} \sum_{<ij>} \tilde{P}_{ij} && (4.5) \\ \tilde{P}_{ij} &= \sum_{\alpha,\beta=1,\alpha\neq\beta}^{N} |\beta\beta\rangle_{ij} \langle\alpha\alpha|_{ij}. && (4.6) \end{aligned}$$

We have put a ˜ on $\tilde{P}_{ij}$ to emphasize that it is not a projection operator. It would have been the SU(N) symmetric projector on the singlet state $|s\rangle_{ij}$ if the condition $\alpha \neq \beta$ were dropped. Having $\alpha \neq \beta$ in $\tilde{P}_{ij}$ is a direct consequence of restricting the sum on a in Eq. (4.4) to off-diagonal generators and is what results in the reduced easy-plane symmetry. This form of the Hamiltonian also makes it apparent that the model is Marshall positive (off-diagonal matrix elements are all negative) and is hence amenable to sign problem free quantum Monte Carlo, just like the fully SU(N) symmetric case. [51]

Now it is straightforward to extend the idea of a four-spin coupling, the so called “Q” interaction [10, 50] to the easy-plane case for any N,

$$H^N_{Q_\perp} = -\frac{Q_\perp}{N^2} \sum_{<ijkl>} \tilde{P}_{ij}\tilde{P}_{kl}, \tag{4.7}$$

where as in the original J-Q model, the sum is taken on both orientations of the bond pairing of the square lattice plaquettes. We note here that for $N = 2$, the $Q_\perp$ term does *not* reduce to H_K, Eq. (4.3). It includes all the terms present there, but contains in addition pair hopping terms that are not present in H_K. Thus $H^N_{J_\perp Q_\perp} \equiv H^N_{J_\perp} + H^N_{Q_\perp}$ provides a new way to cross the superfluid-VBS phase boundary for $N = 2$ and also provides a neat way to extend the four spin interaction to arbitrary N, while still preserving the desired ep-SU(N) symmetry.

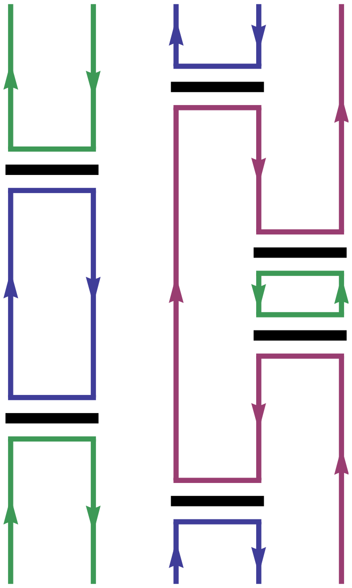

Figure 4.1: A section of a stochastic series expansion configuration of the Hamiltonian, Eq. (4.5), which takes a simple form in terms of N-colored tightly packed oriented closed loops. By “oriented”, we mean an orientation of the links (e.g. shown here as arrows going up on the A sub-lattice and down on the B sub-lattice) can be assigned before any loops are grown, and the orientation remains unviolated by each of the loops in a configuration. The extreme easy-plane anistropy results in an important constraint, *i.e.* loops that share a vertex (operators represented by the black bars) are restricted to have different colors.

4.3 Loop Representation

It turns out that our models has a convenient loop representation in terms of loops in one higher dimension. To see this start with Eq. (4.5) and construct a stochastic series expansion (see Ref. [13] for a comprehensive review). From previous work on similiar models (see e.g. Ref. [52]), we know that the partition function of SU(N) quantum spin Hamiltonians can be viewed as the classical statistical mechanics of N-colors of tightly packed oriented loops in one higher dimension. A section of this particular kind of loop configuration, describing one term in the expansion of the partition function is depicted in FIG. 4.1 for our model. An essential difference from the usual SU(N) case is that loops which are attached to the same vertex (operators represented by the black bars) are restricted to have different colors, which is due to the absence of diagonal matrix elements in Eq. (4.5). This adds an important constraint: whereas in the fully symmetric SU(N) case, given a legal loop configuration loop colors could be assigned independently, in the easy-plane case studied here only a subset of the colorings (the ones that respect the constraint) are allowed. This affects the recoloring of loops in a Monte-Carlo algorithm.

The fact that the loops in our model obey a coloring constraint and that diagonal operators are absent makes this model difficult to simulate as given. This difficulty is overcome, as is commonly done, by shifting the Hamiltonian by a constant. We shift our Hamiltonian in such a way that we introduce diagonal operators with equal weight as the off-diagonal ones. This shift only adds a constant to the energies and does not affect the physics of the model in anyway, i.e. the eigenstates are identical. The shifted Hamiltonian is given by

$$\tilde{H}^{N}_{J_\perp} = -\frac{J_\perp}{N} \sum_{<ij>} (\tilde{P}_{ij} + \mathbb{1}) \tag{4.8}$$

where the diagonal and off-diagonal operators have equal weight. With this shift the directed loop equations [11], describing how the loops pass through a vertex, take on a particularly simple form. We show the loop updating moves and corresponding probabilities in Fig. 4.2. With these rules the loops used to update our QMC configurations are not deterministic, as they are in the SU(N) symmetric case. The loops here can intersect with themselves and one may worry about growing a loop that fails to close onto itself. We have never seen a case of a loop not closing during any of our simulations.

So far we have described our algorithm with $Q_\perp = 0$. The introduction of plaquette operators is easily dealt with if we regard them as simply a product of two (shifted) bond operators. Our algorithm then inserts and removes diagonal plaquette operators, present due to the constant shift, and can convert them to off-diagonal plaquettes by performing loop updates. Since the plaquette operator is viewed as

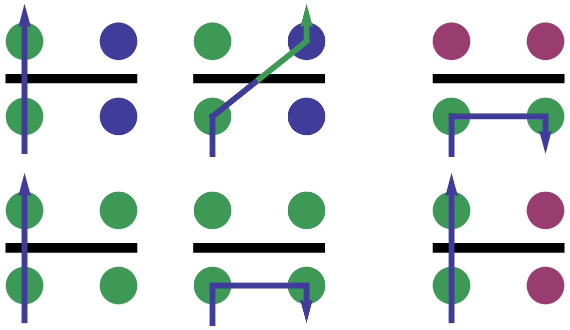

(a) Moves with probability 1/2 (b) Moves with probability 1

Figure 4.2: Loop updating moves describing how loops pass through a vertex, depicted with a black bar. These moves cause conversions between the diagonal and off-diagonal matrix elements present in the Hamiltonian. For each update pictured here there is a reverse process that we have not drawn.

two separate bonds operators, loop updates through the former are the same as for the latter.

4.4 Measurements

Here we will outline the measurements that we use to characterize the phases of our model. On the magnetic side of the transition the spin stiffness, or superfluid stiffness in the language of hard-core bosons, serves as a useful order parameter. It is formally defined as follows:

$$\rho_s = \frac{1}{N_{\text{site}}} \frac{\partial^2 \langle H(\phi) \rangle}{\partial \phi^2}\Big|_{\phi=0} \tag{4.9}$$

where $H(\phi)$ means that we twist the boundary conditions along either the x or y direction. This twist can be implemented, for instance, by attaching phase factors to all x-oriented bond operators relative to one color e.g. $e^{i\phi}|\alpha\alpha\rangle_{ij}\langle\bigcirc\bigcirc|_{ij}$ for $\alpha \neq \bigcirc$, $i \in A$ sublattice and $j \in B$ sublattice. The Hermitian conjugate of this operator appears with $e^{-i\phi}$. Due to the staggered representation, the signs in the exponent are flipped when $i \in B$ and $j \in A$. The bond operators take on this form when the spins are incrementally twisted along the x-direction about the $N-1^{\text{th}}$ diagonal generator

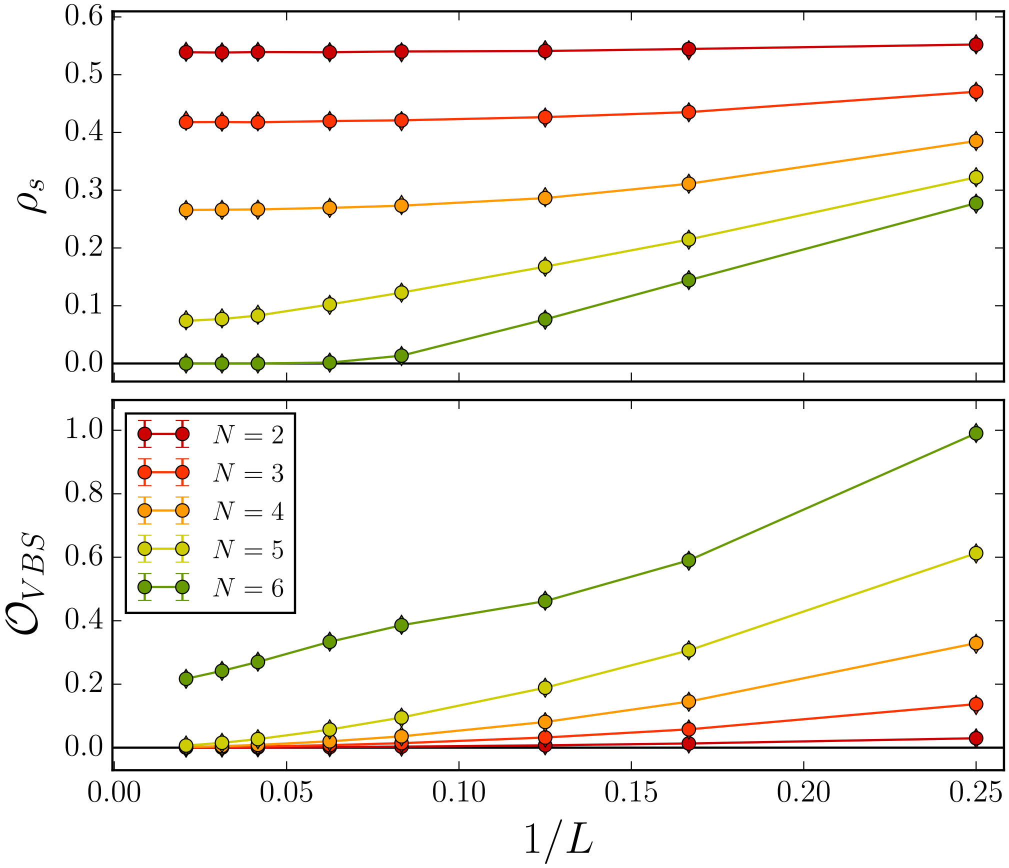

Figure 4.3: The stiffness and VBS order parameter extrapolations as a function of $1/L$ for different N in the nearest neighbor easy-plane model $H^N_{J_\perp}$, defined in Eq. (4.4) or equivalently (4.5). We find clear evidence that the system has superfluid order for all $N \leq 5$ and VBS order for $N > 5$. To show ground state convergence we plot both $\beta = L, 2L$ in diamond and circular points, respectively.

of SU(N). In practice, due to the permutation symmetry of the model, the ◯ color is arbitrary, and we can average over the colors in QMC.

In QMC the stiffness is related to the winding number of configurations via

$$\rho_s = \frac{1}{N_{\text{site}}} \frac{\langle W^2 \rangle}{\beta}, \tag{4.10}$$

where operators with a postive (negative) phase factor count as positive (negative) winding.

In order to characterize the VBS phase, we measure the equal time bond-bond correlation function $\langle \tilde{P}_{\vec{r}\alpha} \tilde{P}_{\vec{r}'\alpha} \rangle$. Here we have denoted a bond by its location on the

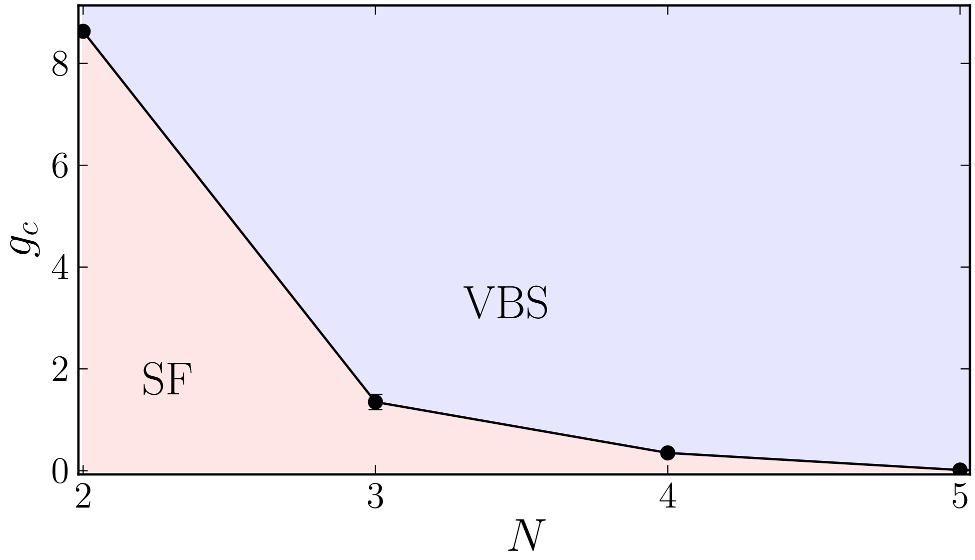

Figure 4.4: Phase diagram of the $H^N_{J_\perp Q_\perp}$ model as a function of the ratio $g_c = Q_\perp/J_\perp$ and N. Using the $H^N_{J_\perp Q_\perp}$ model we have access to the superfluid-VBS phase boundary for $N = 2, 3, 4$ and 5. In this work, we provide clear evidence that the transition for $N = 2$ and $N = 5$ is direct but discontinuous for both order parameters, suggesting that the easy-plane-SU(N) superfluid-VBS transition is generically first order for small-N.

lattice $\vec{r}$ and its orientation α (x or y in two-dimensions). In the VBS phase, lattice translational symmetry is broken giving rise to a Bragg peak in the Fourier transform of the bond-bond correlator defined as

$$\tilde{C}^\alpha(\vec{q}) = \frac{1}{N^2_{\text{site}}} \sum_{\vec{r},\vec{r}'} e^{i(\vec{r}-\vec{r}')\cdot\vec{q}} \langle \tilde{P}_{\vec{r}\alpha} \tilde{P}_{\vec{r}'\alpha} \rangle. \tag{4.11}$$

For columnar VBS patterns, peaks appear at the momenta $(\pi, 0)$ and $(0, \pi)$ for x and y-oriented bonds, respectively. The VBS order parameter is thus given by

$$\mathcal{O}_{VBS} = \frac{\tilde{C}^x(\pi, 0) + \tilde{C}^y(0, \pi)}{2}. \tag{4.12}$$

Another useful quantity that we use to locate phase transitions is the VBS ratio.

$$\mathcal{R}^x_{VBS} = 1 - \tilde{C}^x(\pi + 2\pi/L, 0)/\tilde{C}^x(\pi, 0) \tag{4.13}$$

And similarly for $\mathcal{R}^y_{VBS}$ with all of the q_x and q_y arguments swapped. We then average over x and y- orientations.

$$\mathcal{R}_{VBS} = \frac{\mathcal{R}^x_{VBS} + \mathcal{R}^y_{VBS}}{2}. \tag{4.14}$$

This quantity goes to 1 in a phase with long-range VBS order, and approaches 0 in a phase without VBS order. It is thus a useful crossing quantity that allows us to locate the transition.

To construct these quantities, we measure the equal time bond-bond correlation function in QMC with the following estimator

$$\langle \Theta_1 \Theta_2 \rangle = \frac{1}{\beta^2} \langle (n-1)! N[\Theta_1, \Theta_2] \rangle \tag{4.15}$$

where Θ_1 and Θ_2 are any two QMC operators (in our case off-diagonal bond operators), n is the number of non-null operators in the operator string, and $N[\Theta_1, \Theta_2]$ is the number of times Θ_1 and Θ_2 appear in sequence in the operator string (excluding null slots).

4.5 $J_\perp$-Only Model

Consider the ground state phase of $H^N_{J_\perp}$ as we vary the number of colors N. For $N = 2$ we know the Hamiltonian is equivalent to the quantum XY model, whose ground state is a superfluid. Here it is useful to recall our interpretation of $H^N_{J_\perp}$ as a classical loop model, discussed in Sec. 4.3. In the loop language this corresponds to a long loop phase, where the loops span the system. It is expected that when N is increased the system would like to form as many loops as possible to maximize its entropy, causing it to enter a short loop phase. The way our loop model is defined this will cause the lattice symmetry to break, leading to a VBS and destruction of superfluid order.

Motivated by these considerations, in FIG. 4.3 we plot the spin-stiffness and VBS order parameter for $2 \leq N \leq 6$. We find that the ground state of this Hamiltonian

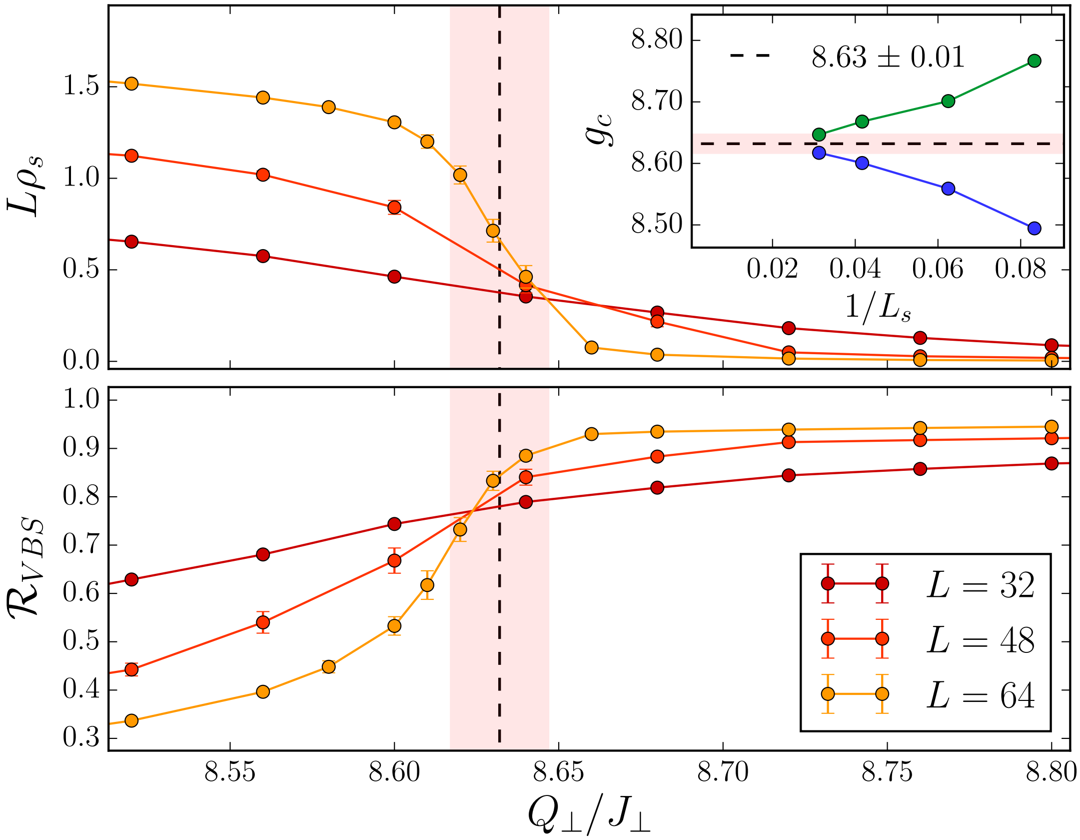

Figure 4.5: Crossings at the SF-VBS quantum phase transition for $N = 2$ in $H^N_{J_\perp Q_\perp}$. The main panels shows the crossings for $L\rho_s$ and $\mathcal{R}_{VBS}$, which signal the destruction and onset of SF and VBS order respectively. The inset shows that the SF-VBS transition is direct, i.e. the destruction of SF order is accompanied by the onset of VBS order at a coupling of $g_c = 8.63(1)$.

has long-range superfluid order for $N \leq 5$ (signalled by a finite spin stiffness) and has VBS order for $N > 5$. These results are obtained by fixing $J_\perp = N, Q_\perp = 0$ and we have plotted two values of inverse temperature $\beta = L, 2L$. On the scale of the plot the two values of β are indistinguishable thus indicating ground state convergence. Since we find magnetic order for $N \leq 5$, we can study the phase transition for these values of N with the introduction of $Q_\perp$.

In conclusion, we find that magnetic order gives way to VBS order in the ep-SU(N) magnet at an N between 5 and 6. In comparison, in the fully SU(N) symmetric case magnetic order is lost between $N = 4$ and 5. [51, 53]

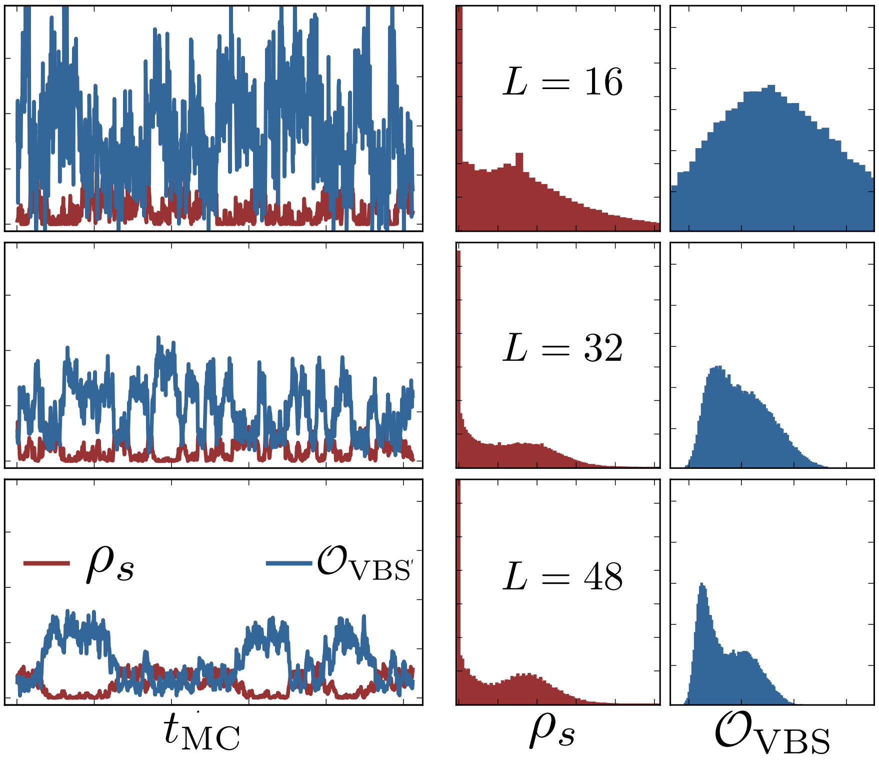

Figure 4.6: Evidence for first order behavior at the SF-VBS quantum phase transition for $N = 2$. The data was collected at a coupling $g_c = 8.63$. The left panel shows MC histories for both ρ_s and $\mathcal{O}_{VBS}$, with clear evidence for switching behavior characteristic of a first order transition. The right panel shows histograms of the same quantities with double peaked structure which gets stronger with system size, again clearly indicating a first order transition.

4.6 $J_\perp$-$Q_\perp$ Model

Through numerical simulations described below we have obtained a phase diagram of the model $H^N_{J_\perp Q_\perp}$, which we show in FIG. 4.4. It is clear that the $Q_\perp$ interaction, which mediates an attraction between the singlets will favor the formation of a VBS state. We confirm this by numerical simulations in which we find that the superfluid order is destroyed at a finite value of $Q_\perp$ for $N = 2$ and gives way to a VBS state. As we increase N, the superfluid order becomes weaker in $H^N_{J_\perp}$, hence requiring only a smaller value of the $Q_\perp$ coupling to destroy the SF order, as is evident from the phase diagram. Finally, as expected for $N > 5$, we are unable to cross the superfluid-VBS phase boundary with $H^N_{J_\perp Q_\perp}$.

We now turn to an analysis of the quantum phase transitions which are denoted by the solid black points in FIG. 4.4. We begin with the case of $N = 2$. FIG. 4.5 shows SU(2) data of our magnetic and VBS crossing quantities, $L\rho_s$ and $\mathcal{R}_{VBS}$. In our data scans we have fixed $J_\perp^2 + Q_\perp^2 = 1$ and have set $\beta = 2L$. Our best estimate for the location of the transition is $Q_\perp/J_\perp = 8.63(1)$. Close to the transition we find that signs of first-order behavior begin to appear. FIG. 4.6 shows the histories of our measurements as a function of Monte Carlo time. We find clear signs that our measurements switch between two values close the transition, an effect which becomes more pronounced at larger system size. Furthermore, binning this data into histograms shows a clear double peaked structure, indicating a first order transition (FIG. 4.6).

First order behavior is observed all the way up to $N = 5$, which is the largest value of N where we can study the transition by tuning $Q_\perp/J_\perp$.

4.7 Conclusions

To summarize, we have introduced a new family of ep-SU(N) models which generalize the XY model of $N = 2$. The generalization preserves the property that it takes only two sites to form a singlet, independent of the value of N. This property is important to the formation of a columnar VBS state. The generalization defines an easy-plane four-spin interaction $Q_\perp$, which allows us to access the superfluid-VBS phase boundary for $N = 2, 3, 4$ and 5. Numerical studies show clear evidence for first order behavior.

How should this observation be interpreted in the terms of the deconfined quantum criticality? In the deconfined criticality scenario the first order transition could either be because the field theory itself does not have a fixed point or if the field theory does have a fixed point, because the quadrupled monopoles are relevant at the fixed point. [54] Given the numerical evidence in the symmetric case that quadrupuled monopoles are irrelevant, we interpret the observed first order behavior here to imply that the non-compact easy-plane deconfined field theory itself is unstable to runaway flow for small-N. This is consistent with direct numerical studies of the easy-plane theory for $N = 2$. [46, 47] Our study raises questions that need to be addressed in future field theoretic and numerical work. Is there a stable large-N easy-plane SU(N) deconfined critical point, or is there a generic reason it does not exist? If it does exist, it is interesting to ask whether numerical simulations will be able to access a large enough N to study this new quantum criticality.

Another interesting topic is the nature of the transition in the ep-SU(N) *without* Berry phases. This study can be numerically achieved by studying our model, Eq. (4.4) on a bilayer square lattice. For $N = 2$ one would expect a 3D XY transition – what happens at larger-N? Previous work on the bilayer SU(N) magnet [55] and classical loop models [56] has shown in the symmetric case that the transition is first order for large enough N, the answer to the same question in the easy-plane case is not known currently and will be pursued in future work.

Chapter 5 Easy-Plane Deconfined Criticality at Large N

This chapter has bee taken from Ref. [57], which has been accepted for publication in the Physical Review Letters.

5.1 Introduction

The emergence of gauge theories in quantum spin Hamiltonians has played an important role in theoretical descriptions of novel magnetic phenomena over the past few decades. Recently, by exploiting advances in simulation algorithms for quantum anti-ferromagnets [1], the connections between magnetism and gauge theories have facilitiated controlled numerical access to otherwise poorly understood strongly coupled gauge theories; the most prominent example is the study of N-component scalar electrodynamics (also called $\mathbb{CP}^{N-1}$) that emerges right at the direct continuous transitions between magnetic and translational-symmetry breaking "valence bond solid" (VBS) states in SU(N) magnets, a phenomena popularly called "deconfined critical points" (DCP) [16].

Two prominent physical systems where the ideas of DCP apply are lattice superfluids and antiferromagnets, each giving rise to its own variant of the $\mathbb{CP}^{N-1}$ theory. In the context of superfluids (SF), the appropriate description is a "easy-plane" $\mathbb{CP}^1$ field theory [16, 17] which applies to the superfluid SF-VBS critical point in $S = 1/2$ XY models [42]. The easy-plane case was studied intensely intially since a self-duality suggested that this could be the best candidate for a DCP [44]. Subsequent numerical work has concluded however that this transition is first order, both in direct discretizations of the field theory [46, 47] as well as in simulations of the quantum anti-ferromagnet [40]. The easy-plane case is in sharp contrast to the case of antiferromagnets with SU(N) symmetry, where striking quantitative agreement between detailed field theoretic calculations [45, 58–60] and numerical simulations has been demonstrated [21, 28, 54].

The persistent first order behavior in the XY-like models and its striking difference from the continuous transitions found in the SU(N) symmetric case has been unexplained so far, despite the central role of both systems in our understanding of the DCP phenomena. In this work we address this issue by formulating an extenstion of the "easy-plane" XY symmetry of SU(2) to general SU(N). Our approach allows for a study of the first order transition for arbirary N using both lattice simulations of an easy plane-SU(N)[ep-SU(N)] model as well as renormalization group (RG) calculations on a proposed easy-plane-$\mathbb{CP}^{N-1}$ [ep-$\mathbb{CP}^{N-1}$]: We find the first order transition in the ep-SU(N) models found for $N = 2$ in previous work persists for larger N. A careful analysis however shows that the first order jump quantitatively weakens as N increases. RG ϵ-expansion calculations find that the field theory hosts a new ep-$\mathbb{CP}^{N-1}$ fixed point only for $N > N_{\text{ep}}$, suggesting that the transition can eventually become continuous. Consistent with this result, we find that the transition in our lattice model turns continuous around $N \approx 20$. For $N = 21$ we provide a detailed scaling analysis of our numerical data that confirms a continuous transition in a new universality class. Our work clarifies and significantly extends the discussion of the DCP phenomena in easy-plane magnets and its relation to the symmetric case.

5.2 Easy-Plane Model & Field Theory

We introduce a family of bipartite ep-SU(N) spin models that are extensions of the quantum XY model to larger N akin to those studied by us recently [40]. They are written in terms of the T_i^a, the fundamental generators of SU(N) on site i:

$$H_{ep} = -\frac{J_{1\perp}}{N} \sum_{a,\langle ij \rangle}{}' T_i^a T_j^{a*} - \frac{J_{2\perp}}{N} \sum_{a,\langle\langle ij \rangle\rangle}{}' T_i^a T_j^a. \tag{5.1}$$

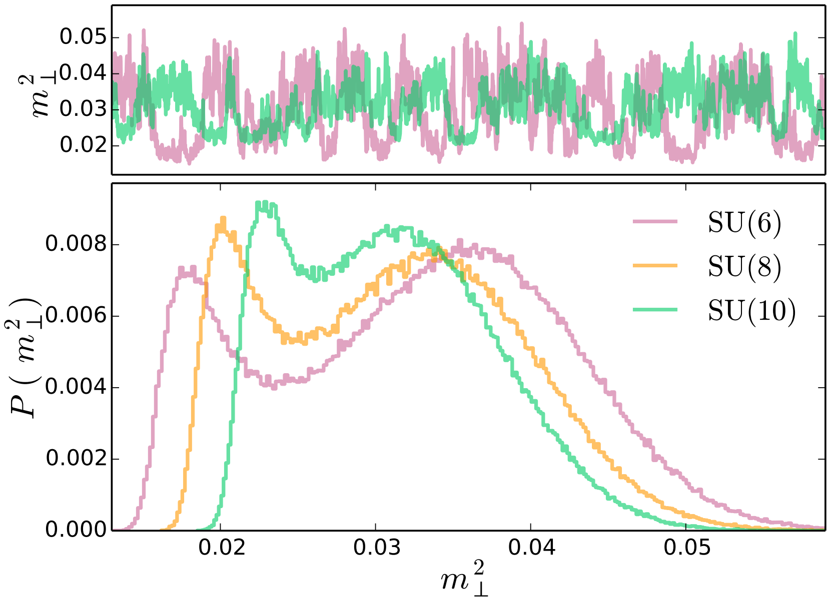

Figure 5.1: First order transitions for moderate values of N. The upper panels shows MC histories (arbitrary units) of the estimator for $m_\perp^2$ for $N = 6$ and 10. The bottom panel shows histograms of $m_\perp^2$ taken at $L = 50$ for $J_2/J_1 \equiv g = 0.250, 0.876, 1.58$ for $N = 6, 8, 10$ respectively clearly show double peaked behavior. The double peaked beahvior persists in the $T = 0$ and thermodynamics limit (see Appendix B.2).

the $\sum'$ denotes the sum on a is restricted to the $N^2 - N$ off-diagonal generators (a sum on all a would give the SU(N) model). The $\langle ij \rangle$ ($\langle\langle ij \rangle\rangle$) indicates nearest (next nearest) neighbors on the square lattice which are on opposite (same) sublattices and in conjugate (same) representations. H_{ep} is an easy plane deformation of the SU(N) J_1-J_2 model [21], it has a global $\mathrm{U}(1)^{N-1} \times \mathrm{S}_N$ (we call this ep-SU(N)) in addition to time reversal and lattice symmetries. As we shall show the model harbors in its phase diagram the SF-VBS transition for all $N > 5$. H_{ep} is Marshall positive for $J_{1\perp}, J_{2\perp} > 0$ (see Appendix B.1); we simulate it with stochastic series Monte Carlo on $L \times L$ lattice at an inverse temperature β [13].

To obtain the effective field theory ($\mathcal{L}_{ep}$) for Eq. 5.1, we start with the $\mathbb{CP}^{N-1}$ model ($\mathcal{L}_s$) proposed to describe DCP in anti-ferromagets with SU(N) symmetry [16, 17] and deform it using an anisotropy operator ($\mathcal{L}_v$), so that $\mathcal{L}_{ep} = \mathcal{L}_s + \mathcal{L}_v$ with,

$$\begin{aligned}
\mathcal{L}_s &= \sum_\alpha |(\partial_\mu - ieA_\mu)z_\alpha|^2 + \frac{1}{2}(\vec{\nabla} \times \vec{A})^2 \\
&+ r\sum_\alpha |z_\alpha|^2 + \frac{u}{2}\left(\sum_\alpha |z_\alpha|^2\right)^2 \\
\mathcal{L}_v &= \frac{v}{2}\sum_\alpha |z_\alpha|^4, \qquad (5.2)
\end{aligned}$$

where the z_α are N complex fields coupled to a U(1) gauge field, A_μ. The term v breaks the SU(N) symmetry of $\mathcal{L}_s$ to the same ep-SU(N) symmetry found above for Eq. 5.1. It is known from the large-N expansion that for N larger than some finite N_s, in $d = 3$ the $\mathbb{CP}^{N-1}$ field theory $\mathcal{L}_s$ has a finite coupling fixed point (FP) [3,61]. Below we will address the fate of these FPs for $\mathcal{L}_{ep}$.

5.3 Weakening First-Order Transition

We begin with a numerical study of Eq. (5.1). We have shown [40] that the ep-SU(N) models map to a certain loop model. We can hence calculate two useful quantities to probe magnetic ordering: the average of the square of the spatial winding number of the loops $\langle W^2 \rangle$ and a normalized magnetic order parameter $m_\perp^2 = \frac{1}{(1-\frac{1}{N})L^4}{\sum_a}' \sum_{i,j} \tilde{T}_i^a \tilde{T}_j^a$ [where the sum on a is on the off-diagonal generators, i and j are summed on the entire lattice and $\tilde{T} = T(T^*)$ on the A(B) sublattice], which although off-diagonal in the $|\alpha\rangle$ basis can be estimated by measuring a particular statistical property of the loops (see Appendix B.2). We have normalized $m_\perp^2$ so that the maximum value it can take is 1 for all N, allowing for a meaningful comparison across different N.

Previously we found that the SF-VBS transtion is first order for $N \leq 5$ [40]. In Fig. 5.1 we present data that shows the first order behavior persists as N is increased up to $N = 10$. A hitherto unanswered but important question is whether the first order jump weakens as N increases. We find evidence in favor of this assertion, since

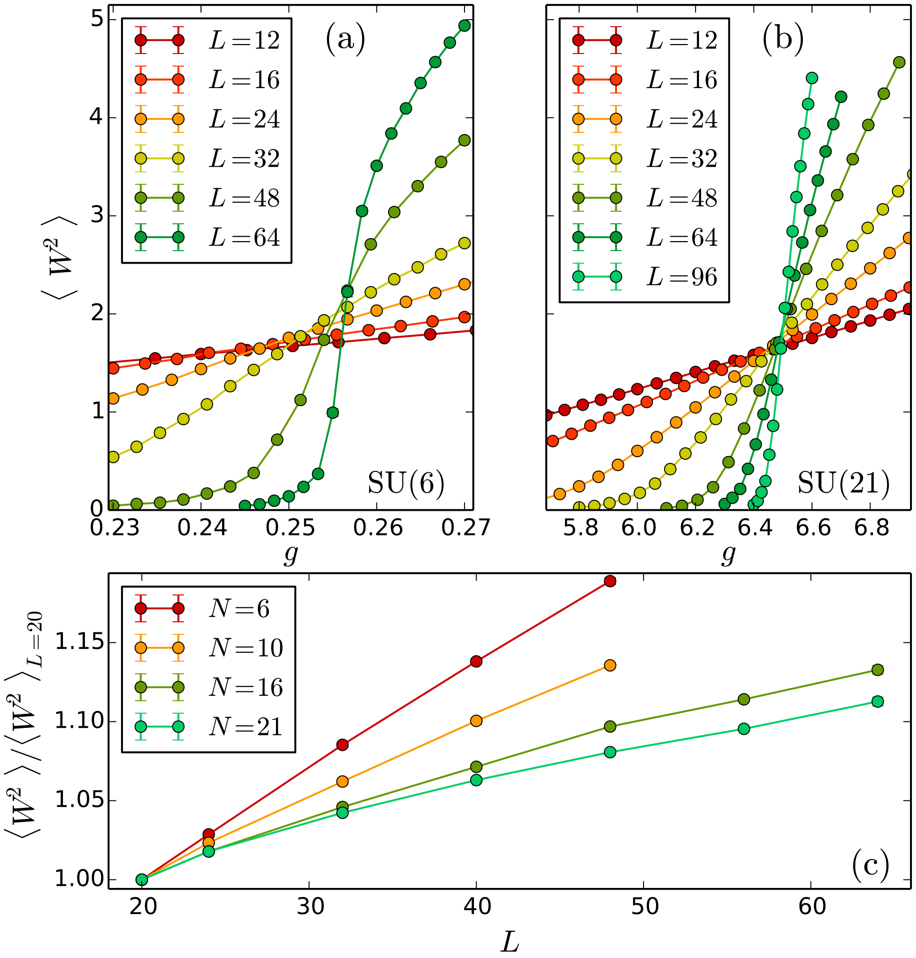

Figure 5.2: Scaling of the spatial winding number square $\langle W^2 \rangle$. (a) Crossing for $N = 6$. (b) Crossing for $N = 21$. (c) Value at the L and $L/2$ crossing of $\langle W^2 \rangle$ for a range of N normalized to the crossing value at $L = 20$ for each N. For the smaller N a clear linear divergence is seen as expected for a first-order transition (ergodicity issues limit the system sizes here). For larger N a slow growth is observed very similar to what has been studied in detail for the SU(2) case and interpreted as evidence for a continuous transition with two length scales [2], like we have here. The data was taken at $\beta = 6L$ which is in the $T = 0$ regime (see Appendix B.2).

the histogram peaks get closer as N is increased. Beyond $N \approx 16$ we have found no evidence for double peaked histograms. To carry out a more quantitative analysis, which has been popular in the study of the DCPs [46], we turn to $\langle W^2 \rangle$ (which is related to the spin stiffness as $\beta\rho_s$). At a first order transition one expects a linear divergence of $\langle W^2 \rangle$ as one approaches the phase transition since ρ_s stays finite. Any sub-linear behavior indicates that the transition is continuous since ρ_s vanishes in the thermodynamic limit [26]. In Fig. 5.2 we present a study of the crossing of $\langle W^2 \rangle$. We find clear evidence for the expected linear behavior at moderate values of N. As N is increased beyond about $N \approx 16$ we find a very slow growth of $\langle W^2 \rangle$ inconsistent with linear behavior but consistent with what has been found in SU(N) models, where the transition is believed to be continuous [2,26]. This study provides clear evidence that the first-order jump decreases as N increases, possibly becoming continuous.

5.4 Renormalization Group Analysis

The weakening of the first-order SF-VBS transitions at larger N raises important questions: Is the transition first order for all N or does it become continuous beyond some finite N_{ep}? If the transition becomes continuous: Is it a new universality class of an ep-$\mathbb{CP}^{N-1}$ or is the anisotropy irrelevant resulting in $\mathbb{CP}^{N-1}$ criticality for the "easy-plane" models?

To answer these questions, we compute the RG flows of Eq. (5.2) in $4-\epsilon$ dimensions. We will work in the critical plane where $r = 0$, the r operator being strongly relevant at tree level will continue to be relevant in the ϵ-expansion. To leading order (assuming u,v and e^2 are $\mathcal{O}(\epsilon)$), we find the following RG equations,

$$\begin{aligned}
\frac{de^2}{d\ln s} &= \epsilon e^2 - \frac{N}{3} e^4, \\
\frac{du}{d\ln s} &= \epsilon u - (N+4)u^2 - 4uv - 6e^4 + 6e^2 u, \\
\frac{dv}{d\ln s} &= \epsilon v - 5v^2 - 6uv + 6e^2 v, \qquad (5.3)
\end{aligned}$$

which for $v = 0$ reduce to the well known RG equations for the $\mathbb{CP}^{N-1}$ model [3,62]. Given the relevance of r, a generic critical point of ep-$\mathbb{CP}^{N-1}$ would be a fixed point of Eq. (5.3) with all three eigen-directions in e^2-u-v-space irrelevant. The FP structure and flows of Eq. 5.3 (shown in Fig. 5.3) change at two values of N: N_s and N_{ep} with

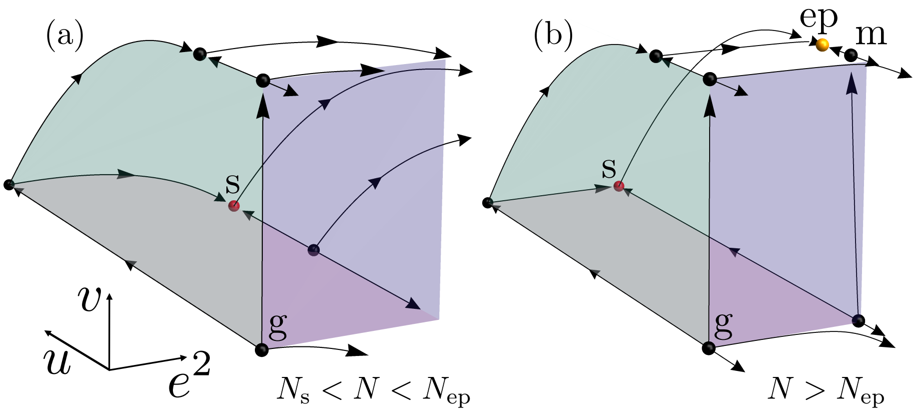

Figure 5.3: RG flows of the ep-$\mathbb{CP}^{N-1}$ model for (a) $N_s < N < N_{ep}$ and (b) $N > N_{ep}$ at leading order in $4 - \epsilon$ dimensions obtained by numerical integration of Eq.(5.3). Fixed points are shown as bold dots, we have only labeled a few significant to our discussion. The flows in the $v = 0$ plane have been obtained previously [3] and include the "s" fixed point that describes DCP in SU(N) models (red dot). While the flows have many FPs, a DCP of the ep-SU(N) spin model must have all three eigen-directions in the e^2-u-v irrelevant. For $N < N_{ep}$ there are no such FPs; there is hence a runaway flow to a first order transition. For $N > N_{ep}$ two FPs emerge: "m" is multicritical and "ep" is the new ep-DCP that describes the SF-VBS transition (yellow dot). The gaussian fixed point at the origin has been labeled "g" for clarity. See Appendix B.4 for further details.

$N_s < N_{ep}$. For $N < N_s$ (not shown) there are no FPs with $e^2 \neq 0$ and a generic flow runs away to a first order transition. For $N > N_s$ a $v = 0$ FP "s" appears, which describes the SU(N) DCP phenomena, but at which v is always relevant. There are two distinct fates of the flow with $v \neq 0$: For $N_s < N < N_{ep}$ (see Fig. 5.3(a)) v causes a runaway flow to a discontinuity FP, i.e. the phase transition turns first order. On the other hand, for $N > N_{ep}$ (see Fig. 5.3(b)) a new fixed point "ep" appears. At this FP all eigen-directions in the $e^2 - u - v$ space are irrelevant and hence r is the only relevant perturbation. "ep" hence describes a generic continuous deconfined SF-VBS transition in models of the form Eq. (5.1). In the leading order of the ϵ-expansion we have $N_s \approx 183$ [3] and $N_{ep} \approx 5363$ (independent of ϵ). From previous work on the symmetric case, it is well known that these leading order estimates are unreliable in $d = 3$: Indeed, in the next to leading order, N_s becomes negative for $\epsilon = 1$ [63, 64]. Ultimately the values of $N_{s,ep}$ must be obtained from numerical

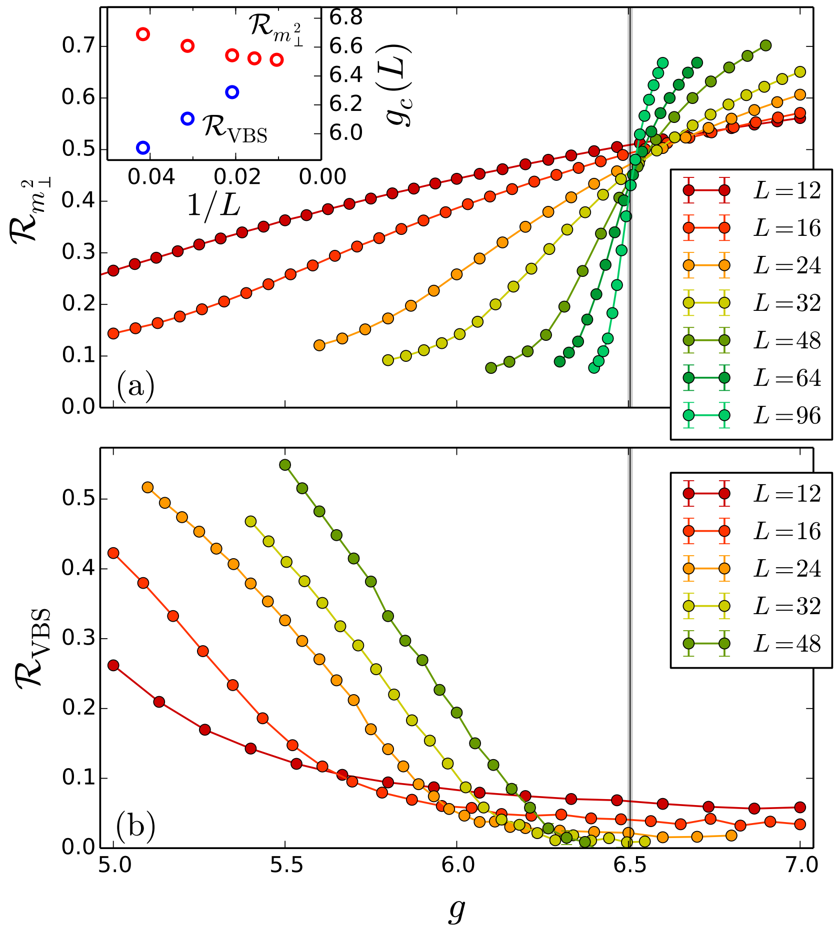

Figure 5.4: Correlation ratios close to the phase transition for $N = 21$. (a) The SF order paramater ratio, $R_{m_\perp^2}$ shows good evidence for a continuous transition with a nicely convergent crossing point of $g = 6.505(5)$. (b) R_{VBS} shows a crossing point that converges to the same value of the critical coupling. We note however that the crossing converges much more slowly (see text). The inset shows the convergence of the crossings points of L and $L/2$ of SF and VBS ratios. Note their convergence to a common critical coupling indicating a direct transition. The data shown in Fig. 5.4 and 5.5 was taken at $\beta = 6L$ which is in the $T = 0$ regime (see Appendix B.2).

simulations. Nonetheless, it is expected that the basic structure of fixed points and flows obtained here using the ϵ-expansion are reliable. Based on our study, we make the following conclusions: Even in a regime where there is a symmetric fixed point ($N > N_s$), for $N_s < N < N_{ep}$, easy-plane anisotropy will drive the DCP first-order. For $N > N_{ep}$ a new FP emerges. Easy-plane anisotropy then results in a continuous

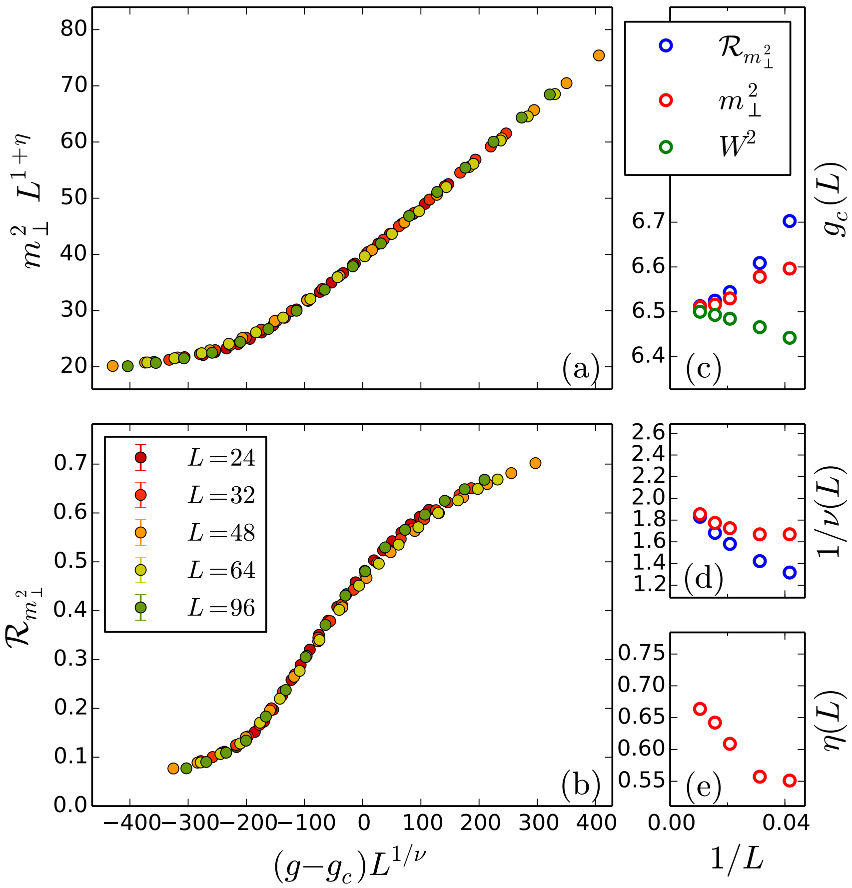

Figure 5.5: Data collapse for the SF order parameter at $N = 21$. (a) Finite size data collapsed to $m_\perp^2 = L^{-(1+\eta_{SF})}\mathbb{M}[(g-g_c)L^{1/\nu}]$ with parameters g_c=6.511, ν=0.556 ($1/\nu$ = 1.795), η=0.652. (b) Collapse of ratio $R_{m_\perp^2} = \mathbb{R}[(g-g_c)L^{1/\nu}]$ with parameters g_c=6.518, ν=0.582 ($1/\nu = 1.719$). The side panels shows convergence of estimates for various quantities from the collapse of L and $L/2$ data: (c) the critical coupling $g_c = 6.505(1)$ from pair-wise collapses of $m_\perp^2$ and $R_{m_\perp^2}$, as well as crossings of $\langle W^2\rangle$ (see Fig. 5.2) for data. Panel (d) shows $1/\nu(L)$, which we estimate to converge to $1/\nu = 2.3(2)$. Likewise we estimate $\eta(L)$ to converge to $\eta = 0.72(3)$, which is shown in panel (e).

SF-VBS transition in a new ep-$\mathbb{CP}^{N-1}$ universality class.

5.5 Study of Fixed Point

Having presented evidence from the ϵ-expansion that with increasing N the transition should turn continuous and in a new universality class, it is of interest to study the scaling behavior at large N. We will focus on $N = 21$ where we have found no evidence for first order behavior on the largest system sizes that we have access to. We construct dimensionless ratios $\mathcal{R}_{m_\perp^2}$ and $\mathcal{R}_{\mathrm{V}BS}$ which go to 1(0) in their respective ordered (disordered) phases. Fig. 5.4 shows our data for $N = 21$. The large correction to scaling observed in the VBS data are expected: according to the DCP theory the VBS anomalous dimension $\eta_{\mathrm{V}BS} \propto N$ which causes the leading VBS correlation functions to decay very rapidly at this large value of N. This makes it hard to separate the leading and sub-leading behavior on the available system sizes. Since the SF data shows a good crossing, we carry out a full scaling analysis in Fig. 5.5. The data for both $m_\perp^2$ and $R_{m_\perp^2}$ collapse nicely without the inclusion of corrections to scaling [65,66]. They lead to consistent values of critical couplings and scaling dimensions lending support for a continuous transition ep-$\mathbb{CP}^{N-1}$ fixed point emerging at large N.

5.6 Conclusion and Outlook

In conclusion, we have studied new lattice models for deconfined criticality with easy-plane SU(N) symmetry. We find persistent first order behavior in these lattice models at small to intermediate N, in sharp contrast to the continuous transitions found in the symmetric models for the same range of N. As N increases the first order easy-plane transition weakens and eventually becomes continuous. Our RG flows provide a way to understand both the first-order and shift to continuous transitions: The easy-plane anisotropy is always relevant at the symmetric $\mathbb{CP}^{N-1}$ fixed point, for $N < N_{ep}$ there is no easy-plane fixed point and hence the anisotropy drives the transition first order. For $N > N_{ep}$ a new fixed point emerges resulting in a continuous transition in a new "easy-plane"-$\mathbb{CP}^{N-1}$ universality class which is an example of a strongly coupled gauge-matter field theory. Our lattice model provides a sign-free discretization of this field theory that is amenable to efficient numerical simulations. We leave for future work the determination of a precise value of N_{ep}, comparisons of the universal quantities with easy-plane large-N expansions, and a comparative study of the scaling corrections between the easy-plane and symmetric cases. It would be of interest to complement our work with studies of field theories such as Eq. (5.2) using the conformal bootstrap [67].

Acknowledgements: We thank G. Murthy for many discussions. Partial financial support was received through NSF DMR-1611161 and the MacAdam fellowship. The numerical simulations reported in the manuscript were carried out on the DLX cluster at the University of Kentucky.

Copyright© Jonathan D'Emidio, 2017.

Appendix A Chapter 4 Supplement

A.1 QMC vs ED

For future reference, Table A.1 contains test comparisons between measurements obtained from a SSE-QMC study and exact diagonalization on 4 × 4 and 4 × 2 systems with various $J_\perp$-$Q_\perp$ at $N = 2$ and $N = 3$. We list values for the ground state energy per site, spin stiffness as in equation (4.9 , 4.10) as well as the VBS order parameter, defined in equation (B.4). For the rectangular systems we have indicated that we use the stiffness in the x-direction and VBS order parameter with x-oriented bonds.

4 × 4	$N = 2$	$J_\perp = 1.0$	$Q_\perp = 0.0$	$\beta_{\text{qmc}} = 48.0$	
e_{ex}	-0.562486	ρ_{ex}	0.27714	$\mathcal{O}_{\text{ex}}$	0.007497
e_{qmc}	$-0.562473(7)$	ρ_{qmc}	0.27710(3)	$\mathcal{O}_{\text{qmc}}$	0.007497(1)
4 × 4	$N = 2$	$J_\perp = 1.0$	$Q_\perp = 1.0$	$\beta_{\text{qmc}} = 32.0$	
e_{ex}	-0.741775	ρ_{ex}	0.35858	$\mathcal{O}_{\text{ex}}$	0.011097
e_{qmc}	$-0.741770(8)$	ρ_{qmc}	0.35860(3)	$\mathcal{O}_{\text{qmc}}$	0.011096(1)
4 × 2	$N = 3$	$J_\perp = 1.0$	$Q_\perp = 0.0$	$\beta_{\text{qmc}} = 32.0$	
e_{ex}	-0.74157	ρ^x_{ex}	0.043932	$\mathcal{O}^x_{\text{ex}}$	0.030816
e_{qmc}	$-0.74158(1)$	ρ^x_{qmc}	0.043928(5)	$\mathcal{O}^x_{\text{qmc}}$	0.030821(3)
4 × 2	$N = 3$	$J_\perp = 1.0$	$Q_\perp = 1.0$	$\beta_{\text{qmc}} = 32.0$	
e_{ex}	-1.25095	ρ^x_{ex}	0.011196	$\mathcal{O}^x_{\text{ex}}$	0.029878
e_{qmc}	$-1.25095(2)$	ρ^x_{qmc}	0.011199(2)	$\mathcal{O}^x_{\text{qmc}}$	0.029878(2)

Table A.1: Test comparisons of measurements from exact diagonalization and finite-T QMC studies for the $N = 2$ and $N = 3$. The energies reported here are per site and the stiffness and VBS order parameters are defined in equations (4.9 , 4.10) and (B.4). For rectangular systems we have used the stiffness along the x-direction and VBS order parameter for x-oriented bonds. All systems have periodic boundary conditions.

A.2 $N = 5$

Here we show our $N = 5$ data which also shows symptoms of first-order behavior. In Fig. A.1 we show the SF-VBS crossings that allow us to determine the critical point. Unlike in the $N = 2$ case, the position of the crossings drifts in the same direction from both the SF and VBS side. Taking finely binned data near the transition again shows us signs of first-order behavior. In Fig. A.2 we show our history and histogram data for $N = 5$. For our largest system size we are able to see significant evidence of a first order transition in both the history and histogram. We note here that unlike in the $N = 2$ case, the location of the transition seems to drift substantially with the system size. This results in only seeing clear signs of on-off switching (indicative of a first-order transition) for our largest system size, although it serves to illustrate

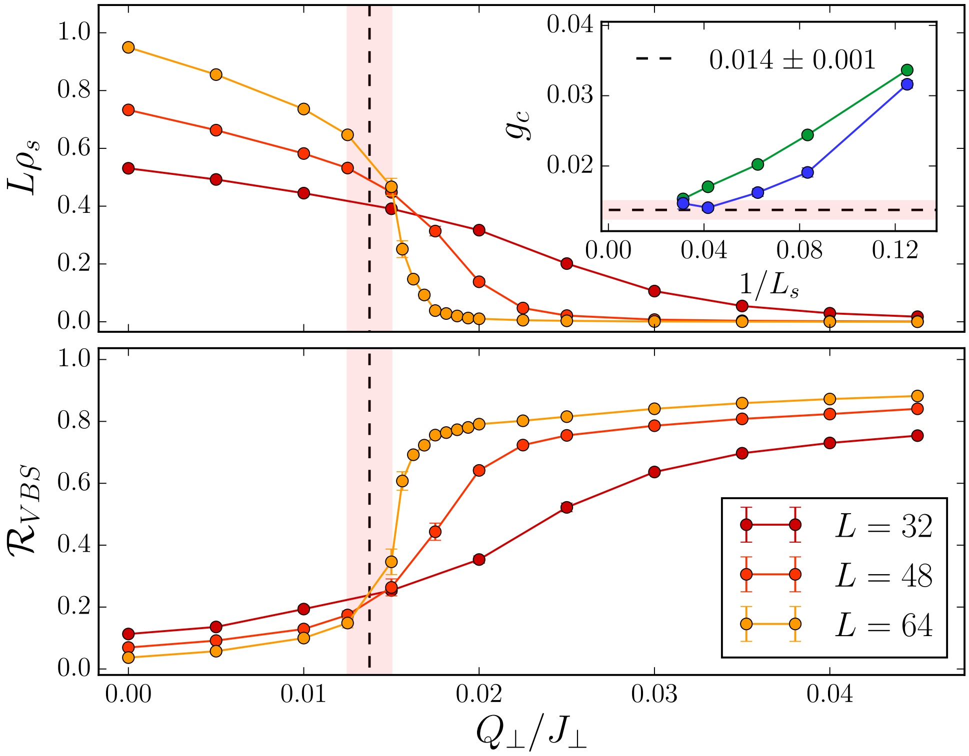

Figure A.1: Crossings at the SF-VBS quantum phase transition for $N = 5$ in $H^N_{J_\perp Q_\perp}$. The main panels shows the crossings for $L\rho_s$ and $\mathcal{R}_{VBS}$, which again show a direct transition between the superfluid and VBS states at $g_c = 0.014(1)$.

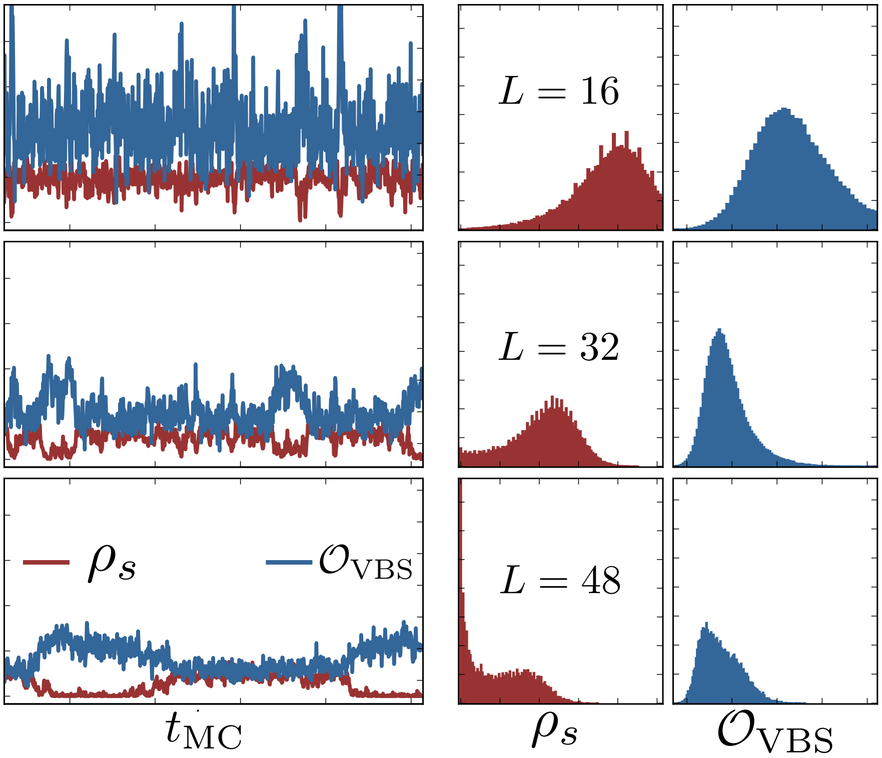

Figure A.2: Evidence for first order behavior at the SF-VBS quantum phase transition for $N = 5$. The data was collected at a coupling $g = 0.01875$. The left panel shows MC histories for both ρ_s and $\mathcal{O}_{VBS}$, with clear evidence for switching behavior characteristic of a first order transition at the largest system size $L = 48$. The right panel shows histograms of the same quantities with double peaked structure emerging at $L = 48$. Here we note that the location of the transition for each system size drifts more significantly than in the $N = 2$ case. Also it can be argued that the transition shows signs of weakening. Here we use a finer bin size for the histories (100 MC sweeps per point).

the presence of a drift. It is arguably the case the the transition is weakening as a function of N given the less pronounced double peaks in the histograms.

Copyright© Jonathan D'Emidio, 2017.

Appendix B Chapter 5 Supplement

B.1 Lattice Hamiltonian

We elaborate on the spin Hamiltonian (5.1), which can be simply written in terms of its matrix elements (choosing the normalization $\mathrm{Tr}[T^a T^b] = \delta_{ab}$)

$$\begin{aligned} H = &-\frac{J_{1\perp}}{N} \sum_{\langle ij \rangle, \alpha, \beta, \alpha \neq \beta} |\alpha_i \alpha_j\rangle\langle\beta_i\beta_j| \\ &-\frac{J_{2\perp}}{N} \sum_{\langle\langle ij \rangle\rangle, \alpha, \beta, \alpha \neq \beta} |\alpha_i \beta_j\rangle\langle\beta_i\alpha_j|, \end{aligned} \tag{B.1}$$

where here we emphasize that α and β are summed from 1 to N with the constraint that $\alpha \neq \beta$. The symmetry of this model is global phase rotations of the form $|\alpha\rangle \to e^{i\theta_\alpha}|\alpha\rangle$, where on one sublattice the phase is conjugated due to the representation. This gives $U(1)^{N-1}$ since an overall phase is trivial. There is also a discrete permutation symmetry S_N that corresponds to a relabeling of the colors. We note that dropping the constraint $\alpha \neq \beta$ restores the full SU(N) symmetry and corresponds to a model already studied in the context of deconfined criticality at large N [21].

This model is explicitly sign free and is amenable to quantum Monte Carlo techniques. We have used the stochastic series expansion QMC algorithm [11], which samples the partition function at finite temperature. For practical implementation, one needs to add a constant to the Hamiltonian in order to generate diagonal matrix elements. We find it convenient to add diagonals with the same weight as the off-diagonals, as follows:

$$\begin{aligned} H \to &-\frac{J_{1\perp}}{N}\sum_{\langle ij\rangle}\left(\sum_{\alpha,\beta,\alpha\neq\beta}|\alpha_i\alpha_j\rangle\langle\beta_i\beta_j| + \mathbb{1}\right) \\ &-\frac{J_{2\perp}}{N}\sum_{\langle\langle ij\rangle\rangle}\left(\sum_{\alpha,\beta,\alpha\neq\beta}|\alpha_i\beta_j\rangle\langle\beta_i\alpha_j| + \mathbb{1}\right). \end{aligned} \tag{B.2}$$

We refer the reader to more details of the loop algorithm contained in [40]. One notable aspect of this $J_{1\perp} - J_{2\perp}$ model is that the addition of the $J_{2\perp}$ term can be treated with minimal extra effort, given a code that simulates $J_{1\perp}$ only. Updating a matrix element (vertex) associated with $J_{2\perp}$ can be achieved by first time reversing the spin states on one sublattice of the vertex, then scattering through the vertex according to the rules for $J_{1\perp}$ matrix elements, and finally reversing the spins back.

B.2 Measurements

Many of our measurements are part of the standard tool kit. This includes the winding number fluctuation $\langle W^2\rangle$, which is related to the superfluid stiffness $\rho = \langle W^2\rangle/\beta$; and also the equal-time bond-bond correlation function, which is used to construct $\mathcal{R}_{\text{VBS}}$. In order to introduce the VBS order parameter and ratio, we first consider the Fourier transformed bond-bond correlator

$$\tilde{C}^a_{VBS}(\vec{q}) = \frac{1}{N^2_{\text{site}}}\sum_{\vec{r},\vec{r}'} e^{i(\vec{r}-\vec{r}')\cdot\vec{q}}\langle\tilde{P}_{\vec{r}a}\tilde{P}_{\vec{r}'a}\rangle, \tag{B.3}$$

where $\tilde{P}_{\vec{r}a}$ is an off-diagonal nearest neighbor bond operator of the form $\sum^N_{\alpha,\beta,\alpha\neq\beta}|\alpha\alpha\rangle_{ij}\langle\beta\beta|_{ij}$ that acts at a bond location $\vec{r}$ with orientation $a \in \{x, y\}$.

For columnar VBS patterns, peaks appear at the momenta $(\pi, 0)$ and $(0, \pi)$ for x and y-oriented bonds, respectively. The VBS order parameter is thus given by

$$\mathcal{O}_{VBS} = \frac{\tilde{C}^x_{VBS}(\pi, 0) + \tilde{C}^y_{VBS}(0, \pi)}{2}. \tag{B.4}$$

We can further construct the VBS ratio, which is defined as

$$\mathcal{R}^x_{VBS} = 1 - \tilde{C}^x_{VBS}(\pi + 2\pi/L, 0)/\tilde{C}^x_{VBS}(\pi, 0) \tag{B.5}$$

And similarly for $\mathcal{R}^y_{VBS}$ with all of the q_x and q_y arguments swapped. We then average over x and y- orientations.

$$\mathcal{R}_{VBS} = \frac{\mathcal{R}^x_{VBS} + \mathcal{R}^y_{VBS}}{2}. \tag{B.6}$$

This quantity goes to 1 in a phase with long-range VBS order, and approaches 0 in the superfluid phase. It is thus a useful crossing quantity that allows us to locate the transition.

To construct these quantities, we measure the equal time bond-bond correlation function in QMC with the following estimator

$$\langle \Theta_1 \Theta_2 \rangle = \frac{1}{\beta^2} \langle (n-1)! N[\Theta_1, \Theta_2] \rangle \tag{B.7}$$

where Θ_1 and Θ_2 are any two QMC operators (in our case off-diagonal nearest neighbor bond operators), n is the number of non-null operators in the operator string, and $N[\Theta_1, \Theta_2]$ is the number of times Θ_1 and Θ_2 appear in sequence in the operator string (excluding null slots).

In this work we have also made use of the less common"in-plane" magnetization $m^2_\perp$, for which we have produced magnetic data collapses. We now outline this particular measurement. The reader is directed to [68] for more details.

The superfluid (magnetic) ordering in our system is off-diagonal in the computational basis, meaning that the relevant equal-time correlation functions are of the form $\langle S^+_i S^-_j \rangle$, written in terms of raising and lowering spin operators. The placement of such an operator into a QMC configuration will in general give zero, unless the two operators are joined by a loop of a certain color. Loop updates can be regarded as

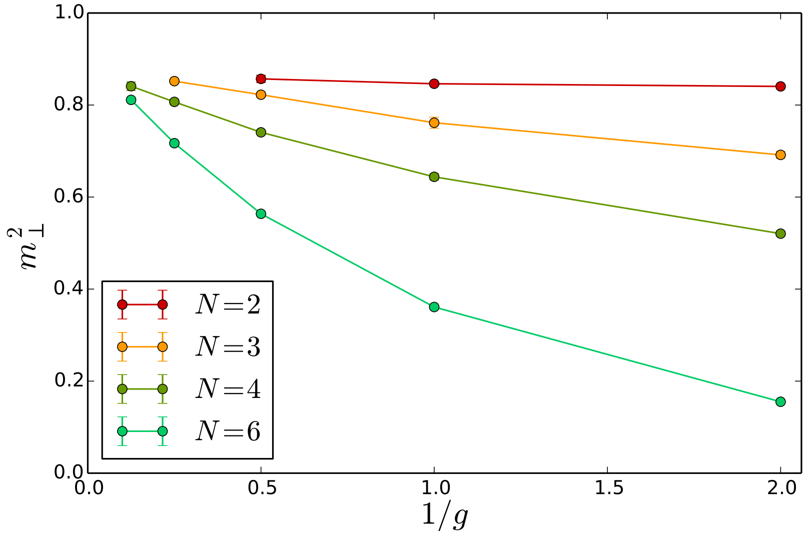

Figure B.1: Maximum values of $m_\perp^2$ deep in the superfluid phase for different values of N. Each data point was obtained by extrapolating the value of $m_\perp^2$ in the thermodynamic limit at a fixed value of the coupling $g = J_{2\perp}/J_{1\perp}$. Increasing g drives the system into the superfluid phase, we can thus observe the maximum possible value of $m_\perp^2$ in the limit $1/g \to 0$. The data is consistent with an upper bound of one.

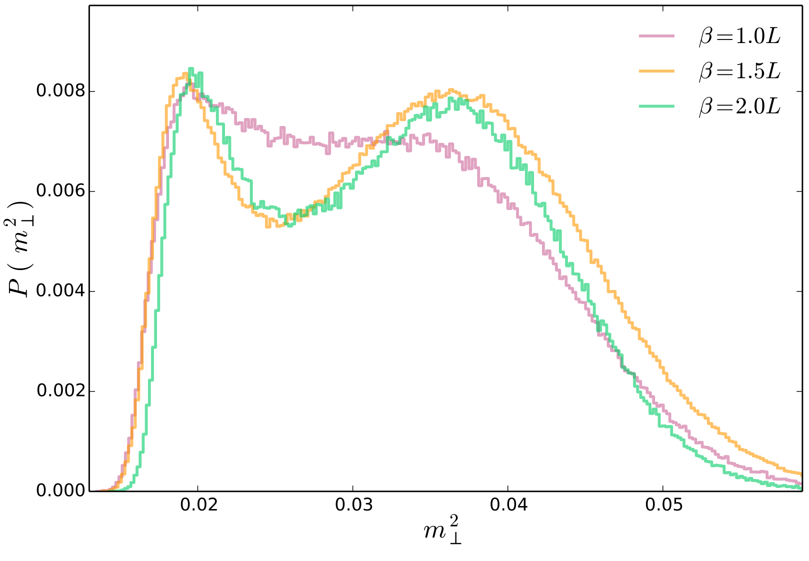

Figure B.2: Histograms of the squared in-plane magnetization for an SU(6) system with $L = 48$ for different values of the inverse temperature β. Once sufficiently low temperatures are reached, such that the two peaks clearly emerge, we find little depedence on temperature as expected.

4×4	$N = 2$	$J_{1\perp} = 1.0$	$J_{2\perp} = 1.0$
e_{ex}	-1.082912818	$m^2_{\perp\text{ex}}$	1.110134109
e_{QMC}	$-1.082909(4)$	$m^2_{\perp\text{QMC}}$	1.11014(1)
4×4	$N = 2$	$J_{1\perp} = 1.0$	$J_{2\perp} = 2.0$
e_{ex}	-1.629091615	$m^2_{\perp\text{ex}}$	1.107517598
e_{QMC}	$-1.629086(5)$	$m^2_{\perp\text{QMC}}$	1.10753(1)
4×2	$N = 3$	$J_{1\perp} = 1.0$	$J_{2\perp} = 1.0$
e_{ex}	-1.131110222	$m^2_{\perp\text{ex}}$	1.408846135
e_{QMC}	$-1.131100(5)$	$m^2_{\perp\text{QMC}}$	1.408849(6)
4×2	$N = 3$	$J_{1\perp} = 1.0$	$J_{2\perp} = 2.0$
e_{ex}	-1.618465034	$m^2_{\perp\text{ex}}$	1.423156633
e_{QMC}	$-1.618476(7)$	$m^2_{\perp\text{QMC}}$	1.423150(8)

Table B.1: QMC versus exact diagonalization. For brevity we provide just the energy per site and normalized $m_\perp^2$ for $N = 2$ and $N = 3$ systems. We have used $\beta = 32$ in our QMC simulations.

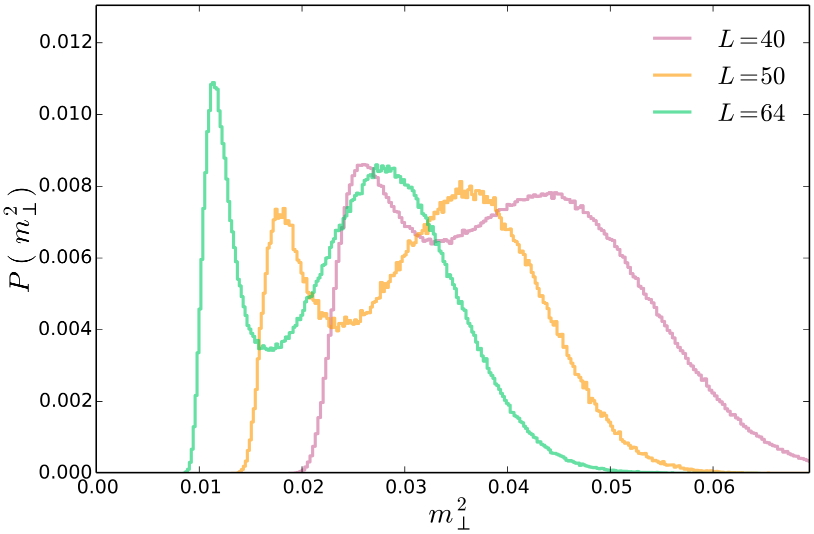

Figure B.3: Hisograms for SU(6) with $\beta = 1.5L$ for different system sizes. The peaks shift toward zero as the system size is increased, reflecting the fact that the magnetization approaches zero as a function of system size near the transition. As the system size is increased the peaks become well separated, indicating thermodynamic first order behavior.

inserting a raising and lowering pair (defects) at the same time slice and spatial location, then propagating one of the defects until it annihilates with the first, forming a closed loop. The algorithm is stochastically sampling the space of allowed config-

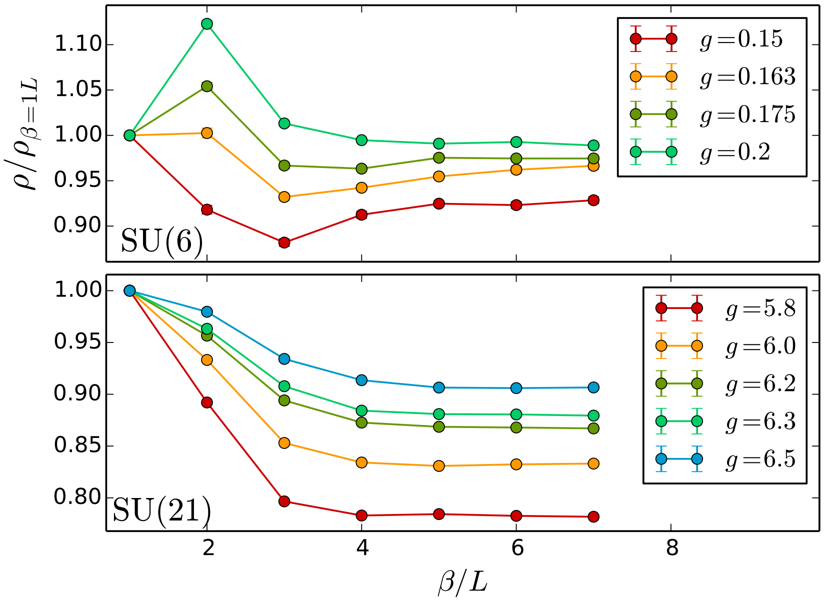

Figure B.4: Convergence of the superfluid stiffness (ρ) as a function of β for $L = 16$ around transition. Finite temperature effects are absent when $\beta \approx 5L$ for both SU(6) and SU(21). We therefore conservatively fix $\beta = 6L$ for the crossing analysis and data collapse presented in the main paper.

urations with two defects. The measurement $\langle S_i^+ S_j^- \rangle$ is then given by the average number of times these two defects occur at the same time slice at locations i and j, which is averaged over the total number of loops grown. We note that starting loops at a vertex leg will bias this measurement, an so it must be performed by choosing a random time slice and spatial location in which to start the loop.

We normalize the (0,0) component of the correlation function to the value $N-1 = \sum_a' T^a T^a$, where the sum on a is on the off-diagonal generators. This is due to the fact that we have chosen $\mathrm{Tr}[T^a T^b] = \delta_{ab}$. We then construct $m_\perp^2$ based on the off-diagonal correlation function as follows:

$$m_\perp^2 = \frac{1}{(1-\frac{1}{N})N_{\mathrm{site}}^2} {\sum_a}' \sum_{i,j} \langle \tilde{T}_i^a \tilde{T}_j^a \rangle \tag{B.8}$$

where i and j are summed on the entire lattice and $\tilde{T} = T(T^*)$ on the A(B) sublattice. In practice we use lattice symmetries to reduce the number of correlators that need to be stored. Here we have importantly chosen an overall normalization factor for $m_\perp^2$ such that the upper bound in the ordered phase is equal to one for all N. The factor $(1-1/N) = (N-1)/N$ accounts for the fact that the generators have been normalized such that the (0,0) component of the correlator is $N-1$ and that, given a color at location 0, the probability of picking the same color at long distances is $1/N$. This amounts to saying that the most magnetically ordered configurations consist of only N loops (one for each color).

The normalization allows us to meaningfully compare this measurement across different values of N and observe a reduction in the size of the first-order jump as in Fig. 5.1. We demonstrate that this normalization is correct in Fig. B.1 by extrapolating the value of $m_\perp^2$ in the thermodynamic limit for different values of $g = J_{2\perp}/J_{1\perp}$.

Analogous to the VBS ratio, we can construct the magnetic ratio as well ($\mathcal{R}_{m_\perp^2}$). If we denote the Fourier transformed off-diagonal spin-spin correlator as

$$\tilde{C}_{m_\perp^2}(\vec{q}) = \frac{1}{(1-\frac{1}{N})N_{\text{site}}^2} {\sum_a}' \sum_{\vec{r},\vec{r}'} e^{i(\vec{r}-\vec{r}')\cdot\vec{q}} \langle \tilde{T}^a_{\vec{r}} \tilde{T}^a_{\vec{r}'} \rangle, \tag{B.9}$$

then the magnetic ratio is then given by

$$\mathcal{R}_{m_\perp^2} = 1 - \frac{\tilde{C}_{m_\perp^2}(2\pi/L,0) + \tilde{C}_{m_\perp^2}(0,2\pi/L)}{2\tilde{C}_{m_\perp^2}(0,0)}. \tag{B.10}$$

We have thoroughly checked all of our measurements against exact diagonalization on small system sizes. In Table B.1 we provide comparisions of the energy per site and normalized $m_\perp^2$ between QMC and exact diagonalization, showing agreement within the statistical error.

We have checked that the behaviour observed in our histograms of the in-plane squared magnetization is qualitatively insensitive with respect to both temperature and system size. In Fig. B.2 we show that the histograms are insenstive to temperature, once sufficiently low temperatures are reached so as to produce two well defined peaks. In Fig. B.3 we show that the peaks become sharper as the system size increased (holding the inverse temperature fixed at $\beta = 1.5L$). We therefore conclude that the behavior is truly first order in nature, and not due to finite size effects.

In order to avoid finite temperature effects in our crossing analysis and data collapse, we fixed $\beta = 6L$ in those simulations. This value was chosen based on the zero temperature convergence of the superfluid stiffness $\rho = \langle W^2 \rangle / \beta$ on an $L = 16$ system size for $N = 6$ and $N = 21$ around the transition. This data is shown in Fig. B.4.

B.3 Renormalization Group Methods

We refer the reader to [62], which is a useful reference that outlines in detail many of the results that we will now discuss. We have performed momentum shell renormalization group transformations in $4 - \epsilon$ dimensions with the Lagrangian density (5.2). We therefore as a starting point write the Euclidean action in $k-$space as follows:

$$\begin{aligned}
S = &\sum_{\alpha} \int \frac{\mathrm{d}\vec{k}}{(2\pi)^d} (\vec{k}^2 + r) z^*_{\alpha}(\vec{k}) z_{\alpha}(\vec{k}) \\
-e &\sum_{\alpha} \int \frac{\mathrm{d}\vec{k}\, \mathrm{d}\vec{p}}{(2\pi)^{2d}} (2\vec{k} + \vec{p}) \cdot \vec{A}(\vec{p}) z^*_{\alpha}(\vec{p} + \vec{k}) z_{\alpha}(\vec{k}) \\
+e^2 &\sum_{\alpha} \int \frac{\mathrm{d}\vec{k}\, \mathrm{d}\vec{p}\, \mathrm{d}\vec{q}}{(2\pi)^{3d}} \vec{A}(\vec{p}) \cdot \vec{A}(\vec{q}) z^*_{\alpha}(\vec{p} + \vec{q} + \vec{k}) z_{\alpha}(\vec{k}) \\
+\frac{1}{2} &\sum_{\alpha,\beta} (u + v\delta_{\alpha\beta}) \int \frac{\mathrm{d}\vec{k}_1 \ldots \mathrm{d}\vec{k}_4}{(2\pi)^{3d}} \delta^d(\vec{k}_1 - \vec{k}_2 + \vec{k}_3 - \vec{k}_4) z^*_{\alpha}(\vec{k}_1) z_{\alpha}(\vec{k}_2) z^*_{\beta}(\vec{k}_3) z_{\beta}(\vec{k}_4) \\
+\frac{1}{2} &\sum_{i,j} \int \frac{\mathrm{d}\vec{k}}{(2\pi)^d} A_i(\vec{k}) [\vec{k}^2 (\delta_{ij} - \hat{k}_i \hat{k}_j) + \frac{k_i k_j}{\xi}] A_j(-\vec{k}).
\end{aligned} \tag{B.11}$$

Here we have used the standard Faddeev-Popov gauge fixing trick, with gauge fixing parameter ξ [69]. Fig. B.5 shows the interaction vertices that couple the slow and fast Fourier modes, where the slow modes (to be denoted schematically by $z_<$ and $A_<$) have momenta in the range $0 < |\vec{k}| < \Lambda/s$ and the fast modes ($z_>$ and $A_>$) have momenta $\Lambda/s < |\vec{k}| < \Lambda$.

The partition function is separated according to fast and slow modes and the contribution from the fast modes is evaluated perturbatively assuming u, v and e^2 are all of order ϵ.

$$Z = \int \mathcal{D}z^*_<\mathcal{D}z_<\mathcal{D}A_< e^{-S_<} \int \mathcal{D}z^*_>\mathcal{D}z_>\mathcal{D}A_> e^{-(V_{<,>}+V_{>,>})} e^{-S_{0,>}}. \tag{B.12}$$

We have separated out the part of the action which only depends on the slow modes ($S_<$), as well as interaction terms in S which mix slow and fast ($V_{<,>}$) and interactions for the fast modes ($V_{>,>}$). Additionally, the part of the action that is quadratic in the fast modes ($S_{0,>}$) is explicitly seperated out. The average $\langle e^{-(V_{<,>}+V_{>,>})}\rangle_{0,>}$ can then be computed perturbatively using the cumulant expansion. This leads to a renormalization of the terms in $S_<$. To first order in ϵ the renormalized action for the slow modes ($S'_<$) looks like

$$\begin{aligned}
S'_< =& \sum_\alpha \int_0^{\Lambda/s} \frac{\mathrm{d}\vec{k}}{(2\pi)^d} (\mathcal{Z}_\eta \vec{k}^2 + \mathcal{Z}_r r) z^*_\alpha(\vec{k}) z_\alpha(\vec{k}) \\
-\mathcal{Z}_\eta e & \sum_\alpha \int_0^{\Lambda/s} \frac{\mathrm{d}\vec{k}\,\mathrm{d}\vec{p}}{(2\pi)^{2d}} (2\vec{k}+\vec{p})\cdot\vec{A}(\vec{p}) z^*_\alpha(\vec{p}+\vec{k}) z_\alpha(\vec{k}) \\
+\mathcal{Z}_\eta e^2 & \sum_\alpha \int_0^{\Lambda/s} \frac{\mathrm{d}\vec{k}\,\mathrm{d}\vec{p}\,\mathrm{d}\vec{q}}{(2\pi)^{3d}} \vec{A}(\vec{p})\cdot\vec{A}(\vec{q}) z^*_\alpha(\vec{p}+\vec{q}+\vec{k}) z_\alpha(\vec{k}) \\
& + \frac{1}{2}\sum_{\alpha,\beta}(u' + v'\delta_{\alpha\beta}) \int_0^{\Lambda/s} \frac{\mathrm{d}\vec{k}_1\ldots\mathrm{d}\vec{k}_4}{(2\pi)^{3d}} \delta^d(\vec{k}_1 - \vec{k}_2 + \vec{k}_3 - \vec{k}_4) z^*_\alpha(\vec{k}_1) z_\alpha(\vec{k}_2) z^*_\beta(\vec{k}_3) z_\beta(\vec{k}_4) \\
& + \frac{1}{2}\sum_{i,j} \int_0^{\Lambda/s} \frac{\mathrm{d}\vec{k}}{(2\pi)^d} A_i(\vec{k}) [\mathcal{Z}_A \vec{k}^2(\delta_{ij} - \hat{k}_i\hat{k}_j) + \frac{k_i k_j}{\xi}] A_j(-\vec{k}),
\end{aligned} \tag{B.13}$$

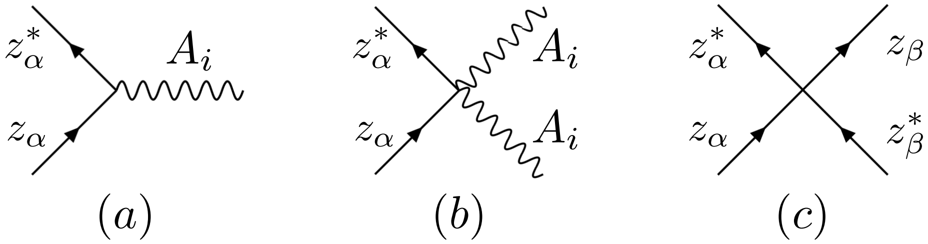

Figure B.5: Interaction vertices that couple fast and slow modes. Perturbative RG is carried out to first order in ϵ by forming all possible one loop diagrams from these vertices.

where

$$\begin{aligned}
\mathcal{Z}_\eta &= 1 - 3\hat{e}^2 \ln(s) \\
\mathcal{Z}_r &= 1 - [(N+1)\hat{u} + 2\hat{v}]\ln(s) \\
\mathcal{Z}_A &= 1 + \frac{1}{3}N\hat{e}^2 \ln(s) \\
\hat{u}' &= \hat{u} - [(N+4)\hat{u}^2 + 4\hat{u}\hat{v} + 6\hat{e}^4]\ln(s) \\
\hat{v}' &= \hat{v} - [5\hat{v}^2 + 6\hat{u}\hat{v}]\ln(s).
\end{aligned} \tag{B.14}$$

Here we have defined dimensionless couplings $\hat{g} \equiv g\Lambda^{d-4}\mathcal{S}_d/(2\pi)^d$ with $\mathcal{S}_d$ being the surface area of a $d-$dimensional sphere and $g = e^2, u, v$. We have used Landau gauge $\xi = 0$ (which forces $\vec{\nabla} \cdot \vec{A} = 0$) in order to evaluate loop integrals involving the gauge field propagator. We now rescale the momentum: $\vec{k} \to \vec{k}/s$ and fields $z_\alpha(\vec{k}/s) \to s^{(d/2+1)}\mathcal{Z}_\eta^{-1/2} z_\alpha(\vec{k})$, $\vec{A}(\vec{k}/s) \to s^{(d/2+1)}\mathcal{Z}_A^{-1/2}\vec{A}(\vec{k})$. This defines the renormalized couplings as $r(s) = \mathcal{Z}_r s^2 r/\mathcal{Z}_\eta$, $u(s) = u' s^\epsilon/\mathcal{Z}_\eta^2$, $v(s) = v' s^\epsilon/\mathcal{Z}_\eta^2$ and $e^2(s) = e^2 s^\epsilon/\mathcal{Z}_A$. With the renormalized couplings we can now write the $\beta-$

functions:

$$\frac{dr}{d\ln s} = r[2-(N+1)u-2v+3e^2] \tag{B.15a}$$
$$\frac{de^2}{d\ln s} = \epsilon e^2 - \frac{N}{3}e^4 \tag{B.15b}$$
$$\frac{du}{d\ln s} = \epsilon u-(N+4)u^2-4uv-6e^4+6e^2u \tag{B.15c}$$
$$\frac{dv}{d\ln s} = \epsilon v-5v^2-6uv+6e^2v. \tag{B.15d}$$

We note that when $N = 1$, these equations have the the same form for v as for u. This is a useful check, as the v term is identical to the u term when $N = 1$. A drawback of the momentum shell approach is that the momentum cutoff breaks gauge invariance, and hence we have discarded terms that would renormalize ξ. The field theoretic RG formulation preserves gauge invariance, and we have checked that out β-functions match using this approach as well.

B.4 RG Flow Equations

Here we will elaborate on the structure of the RG flow equations that have been presented in the main text. Throughout this discussion, we will take $r = 0$, working in the critical plane. Equation (B.15b) can be set to zero and solved to find the fixed point values of e^2. This gives us both charged and uncharged fixed points, $e^2 = 0$ and $e^2 = 3\epsilon/N$. There are always four real fixed points with $e^2 = 0$, which are given by:

$$e^2 = 0 \quad u = 0 \qquad v = 0 \tag{B.16a}$$
$$e^2 = 0 \quad u = \frac{\epsilon}{N+4} \qquad v = 0 \tag{B.16b}$$
$$e^2 = 0 \quad u = 0 \qquad v = \frac{\epsilon}{5} \tag{B.16c}$$
$$e^2 = 0 \quad u = \frac{\epsilon}{5N-4} \qquad v = \frac{(N-2)\epsilon}{5N-4}. \tag{B.16d}$$

These fixed points are identified (see [70]) as Gaussian (B.16a), Wilson-Fisher or Heisenberg (B.16b), Ising (B.16c), and cubic (B.16d) fixed points. Note that the z fields can be separated into their real and imaginary parts, and when $v = 0$ the same fixed point structure appears as in the $O(2N)$ field theory with quartic interaction $(\sum_\alpha^{2N} \phi_\alpha \phi_\alpha)^2$. The addition of v breaks the $O(2N)$ symmetry of the model, since it contains the interaction $\sum_\alpha^{2N} \phi_\alpha^4$, which is typically referred to as cubic anisotropy. The other fixed point with $v \neq 0$, $u = 0$ is referred to as the Ising fixed point, since it corresponds to $2N$ independent copies of the Ising field theory.

It is well known that in the $O(n)$ model (to first order in ϵ) the Wilson-Fisher fixed point is stable for $n < 4$, and for $n > 4$ the cubic fixed point becomes the only stable one. In our case $2N = n$, and we indeed observe exactly this behavior in our flow equations below and above $N = 2$.

We now go on to discuss the fixed points when $e^2 = 3\epsilon/N$. The two fixed points with $v = 0$ are given by:

$$\begin{aligned} e^2 &= 3\epsilon/N \\ u_\pm &= \frac{\epsilon}{2N(N+4)} \left(N + 18 \pm \sqrt{(N+18)^2 - 216(N+4)} \right) \\ v &= 0. \end{aligned} \tag{B.17}$$

These two fixed points become real when $N > 182.9516 = N_\mathrm{s}$. Of these, the fixed point at u_+ is the symmetric deconfined fixed point, which is stable in the $r = 0, v = 0$ plane. The multicritical point at u_- has one relevant direction in the $r = 0, v = 0$ plane. We note that when $v \neq 0$, this causes a runaway flow from the deconfined fixed point, which shows up as a first order transition in our lattice simulations. For this value of N (corresponding to panel (a) of Fig. B.6) there are no stable fixed points in the $r = 0$ plane.

We now move to the final fixed points that appear as N is increased even further, which is the main result of this paper. This corresponds to the finite solution for v

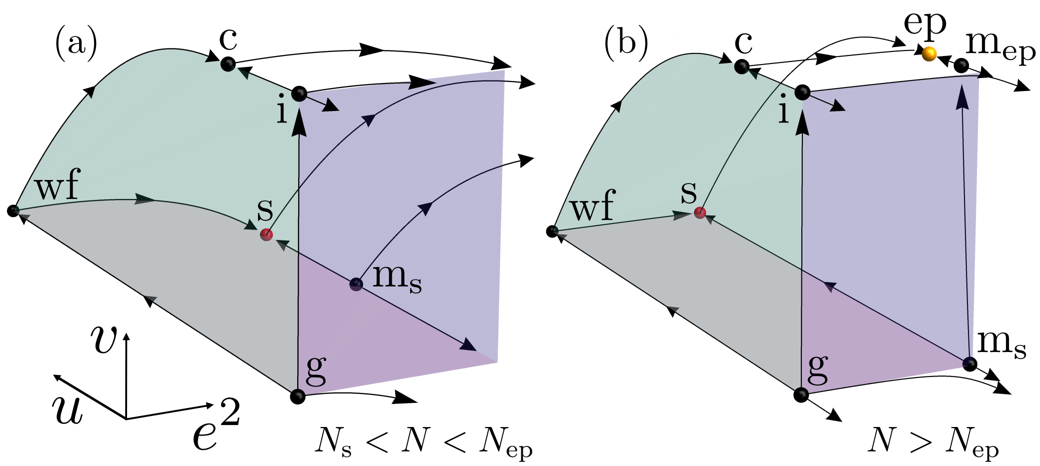

Figure B.6: Here we show our flow diagrams for $N_\mathrm{s} < N < N_\mathrm{ep}$ and $N > N_{ep}$, this time with all of the fixed points marked. The labels correspond to Gaussian (g), Wilson-Fisher (wf), Ising (i), cubic (c), symmetric deconfined (s), symmetric multicritical ($\mathrm{m_s}$), easy-plane deconfined (ep) and easy-plane multicritical ($\mathrm{m_{ep}}$). ep is the only fixed point with all directions irrelevant in the $r = 0$ plane.

in Eqn (B.15d)

$$\begin{aligned} e^2 &= 3\epsilon/N \\ u_\pm &= \frac{\epsilon}{2N(5N-4)}\left(N + 18 \pm \sqrt{(N+18)^2 - 1080(5N-4)}\right) \\ v_\pm &= \frac{1}{5}\left[\epsilon\left(1 + 18/N\right) - 6u_\pm\right] \end{aligned} \tag{B.18}$$

Here the solutions for u (and hence the solutions for v) become real when $N > 5363.1341 = N_\mathrm{ep}$. The solution at u_+ is the easy-plane deconfined fixed point, which has all directions irrelevant in the $r = 0$ plane and is hence stable. The other solution at u_- is a multicritical point denoted by m_ep in Fig. B.6. The easy-plane deconfined fixed point describes the criticality observed in our lattice model at large N.

We note at this point that the values of N_s and N_{ep} obtained from the ϵ expansion at first order are notoriously unreliable. The value of N_s is believed to extend all the way down to $N = 2$ based on the observed deconfined criticality in spin-1/2 systems [1]. Likewise we observe $N_\mathrm{ep} \approx 20$ from our lattice simulations. It is interesting to note that the ϵ expansion gives N_ep that is an order of magnitude larger than N_s, which is observed in numerical simulations.

Copyright© Jonathan D'Emidio, 2017.

References

[1] R. K. Kaul, R. G. Melko, and A. W. Sandvik. Bridging lattice-scale physics and continuum field theory with quantum monte carlo simulations. *Annu. Rev. Cond. Matt. Phys*, 4:179, 2013.

[2] Hui Shao, Wenan Guo, and Anders W. Sandvik. Quantum criticality with two length scales. *Science*, 352(6282):213–216, 2016.

[3] B. I. Halperin, T. C. Lubensky, and Shang-keng Ma. First-order phase transitions in superconductors and smectic-a liquid crystals. *Phys. Rev. Lett.*, 32(6):292–295, Feb 1974.

[4] Michael Fowler. *Historical Beginnings of Theories of Electricity and Magnetism*, 1995 (accessed April 20, 2017). `http://galileoandeinstein.physics.virginia.edu/more_stuff/E&M_Hist.html`.

[5] Jennifer Ouellette Nadia Ramlagan Alan Chodos, Ernie Tretkoff. *APS News - This Month in Physics History, July 1820: Oersted and electromagnetism*, 1995 (accessed April 20, 2017). `https://www.aps.org/publications/apsnews/200807/physicshistory.cfm`.

[6] N. F. Kharchenko. On seven decades of antiferromagnetism. *Low Temperature Physics*, 31(8):633–634, 2005.

[7] Patrick A. Lee, Naoto Nagaosa, and Xiao-Gang Wen. Doping a mott insulator: Physics of high-temperature superconductivity. *Rev. Mod. Phys.*, 78:17–85, Jan 2006.

[8] Leon Balents. Spin liquids in frustrated magnets. *Nature*, 464(7286):199–208, 03 2010.

[9] S. Sachdev. *Quantum Phase Transitions.* Cambridge University Press, 1999.

[10] Anders W. Sandvik. Evidence for deconfined quantum criticality in a two-dimensional heisenberg model with four-spin interactions. *Phys. Rev. Lett.*, 98:227202, Jun 2007.

[11] Olav F. Syljuåsen and Anders W. Sandvik. Quantum monte carlo with directed loops. *Phys. Rev. E*, 66(4):046701, Oct 2002.

[12] Anders W. Sandvik. Ground state projection of quantum spin systems in the valence-bond basis. *Phys. Rev. Lett.*, 95:207203, Nov 2005.

[13] Anders W. Sandvik. Computational studies of quantum spin systems. *AIP Conference Proceedings*, 1297(1):135–338, 2010.

[14] L. D. Landau, E. M. Lifshitz, and E. M. Pitaevskii. *Statistical Physics*. Butterworth- Heinemann, New York, 1999.

[15] Kenneth G. Wilson and J. Kogut. The renormalization group and the ϵ-expansion. *Physics Reports*, 12(2):75 – 199, 1974.

[16] T. Senthil, Ashvin Vishwanath, Leon Balents, Subir Sachdev, and Matthew P. A. Fisher. Deconfined quantum critical points. *Science*, 303(5663):1490–1494, 2004.

[17] T. Senthil, Leon Balents, Subir Sachdev, Ashvin Vishwanath, and Matthew Fisher. Quantum criticality beyond the landau-ginzburg-wilson paradigm. *Phys. Rev. B*, 70:144407, Oct 2004.

[18] Anders W. Sandvik. Continuous quantum phase transition between an antiferromagnet and a valence-bond solid in two dimensions: Evidence for logarithmic corrections to scaling. *Phys. Rev. Lett.*, 104(17):177201, Apr 2010.

[19] F. Jiang, M. Nyfeler, S. Chandrasekharan, and U. Wiese. From an antiferromagnet to a valence bond solid: evidence for a first-order phase transition. *J. Stat. Mech.: Theory and Experiment*, 2008:02009, 2008.

[20] A. Kuklov, M. Matsumoto, N. Prokof'ev, B. Svistunov, and M. Troyer. Deconfined criticality: Generic first-order transition in the su(2) symmetry case. *Phys. Rev. Lett.*, 101:050405, Aug 2008.

[21] R. K. Kaul and A. W. Sandvik. Lattice model for the SU(n) néel to valence-bond solid quantum phase transition at large n. *Phys. Rev. Lett.*, 108:137201, Mar 2012.

[22] Ian Affleck. Large-n limit of SU(n) quantum "spin" chains. *Phys. Rev. Lett.*, 54:966–969, Mar 1985.

[23] Ribhu K Kaul and Matthew S Block. Numerical studies of various nel-vbs transitions in su(n) anti-ferromagnets. *Journal of Physics: Conference Series*, 640(1):012041, 2015.

[24] Matthew P. A. Fisher, Peter B. Weichman, G. Grinstein, and Daniel S. Fisher. Boson localization and the superfluid-insulator transition. *Phys. Rev. B*, 40:546–570, Jul 1989.

[25] Andrey V. Chubukov, Subir Sachdev, and Jinwu Ye. Theory of two-dimensional quantum heisenberg antiferromagnets with a nearly critical ground state. *Phys. Rev. B*, 49:11919–11961, May 1994.

[26] Ribhu K. Kaul. Quantum criticality in su(3) and su(4) antiferromagnets. *Phys. Rev. B*, 84(5):054407, Aug 2011.

[27] Kun Chen, Yuan Huang, Youjin Deng, A. B. Kuklov, N. V. Prokof'ev, and B. V. Svistunov. Deconfined criticality flow in the heisenberg model with ring-exchange interactions. *Phys. Rev. Lett.*, 110:185701, May 2013.

[28] Adam Nahum, P. Serna, J. T. Chalker, M. Ortuño, and A. M. Somoza. Emergent so(5) symmetry at the néel to valence-bond-solid transition. *Phys. Rev. Lett.*, 115:267203, Dec 2015.

[29] N. Read and Subir Sachdev. Large- N expansion for frustrated quantum antiferromagnets. *Phys. Rev. Lett.*, 66:1773–1776, Apr 1991.

[30] Bill Sutherland. Model for a multicomponent quantum system. *Phys. Rev. B*, 12:3795–3805, Nov 1975.

[31] N. Read and Subir Sachdev. Valence-bond and spin-peierls ground states of low-dimensional quantum antiferromagnets. *Phys. Rev. Lett.*, 62:1694–1697, Apr 1989.

[32] Congjun Wu. Exotic many-body physics with large-spin fermi gases. *Physics*, 3:92, Nov 2010.

[33] Ribhu K. Kaul. Spin nematics, valence-bond solids, and spin liquids in SO(n) quantum spin models on the triangular lattice. *Phys. Rev. Lett.*, 115:157202, Oct 2015.

[34] Eugene Demler, Werner Hanke, and Shou-Cheng Zhang. $SO(5)$ theory of antiferromagnetism and superconductivity. *Rev. Mod. Phys.*, 76:909–974, Nov 2004.

[35] Ribhu K. Kaul. Spin nematic ground state of the triangular lattice $s = 1$ biquadratic model. *Phys. Rev. B*, 86:104411, Sep 2012.

[36] Tarun Grover and T. Senthil. Quantum spin nematics, dimerization, and deconfined criticality in quasi-1d spin-one magnets. *Phys. Rev. Lett.*, 98(24):247202, Jun 2007.

[37] Cenke Xu and Leon Balents. Quantum phase transitions around the staggered valence-bond solid. *Phys. Rev. B*, 84:014402, Jul 2011.

[38] Michael Levin and Xiao-Gang Wen. Detecting topological order in a ground state wave function. *Phys. Rev. Lett.*, 96:110405, Mar 2006.

[39] Alexei Kitaev and John Preskill. Topological entanglement entropy. *Phys. Rev. Lett.*, 96:110404, Mar 2006.

[40] Jonathan D'Emidio and Ribhu K. Kaul. First-order superfluid to valence-bond solid phase transitions in easy-plane SU(n) magnets for small n. *Phys. Rev. B*, 93:054406, Feb 2016.

[41] Ashvin Vishwanath and T. Senthil. Physics of three-dimensional bosonic topological insulators: Surface-deconfined criticality and quantized magnetoelectric effect. *Phys. Rev. X*, 3:011016, Feb 2013.

[42] A. W. Sandvik, S. Daul, R. R. P. Singh, and D. J. Scalapino. Striped phase in a quantum xy model with ring exchange. *Phys. Rev. Lett.*, 89:247201, Nov 2002.

[43] A. W. Sandvik and R. Melko. Nature of the antiferromagnetic to valence-bond-solid quantum phase transition in a 2d xy-model with four-site interactions. *http://arxiv.org/abs/cond-mat/0604451*, 2006.

[44] Olexei I. Motrunich and Ashvin Vishwanath. Emergent photons and transitions in the O(3) sigma model with hedgehog suppression. *Phys. Rev. B*, 70:075104, Aug 2004.

[45] T. Senthil and Matthew P. A. Fisher. Competing orders, nonlinear sigma models, and topological terms in quantum magnets. *Phys. Rev. B*, 74:064405, Aug 2006.

[46] A.B. Kuklov, N.V. Prokofev, B.V. Svistunov, and M. Troyer. Deconfined criticality, runaway flow in the two-component scalar electrodynamics and weak first-order superfluid-solid transitions. *Annals of Physics*, 321(7):1602 – 1621, 2006. July 2006 Special Issue.

[47] S. Kragset, E. Smørgrav, J. Hove, F. S. Nogueira, and A. Sudbø. First-order phase transition in easy-plane quantum antiferromagnets. *Phys. Rev. Lett.*, 97:247201, Dec 2006.

[48] S. V. Isakov, S. Wessel, R. G. Melko, K. Sengupta, and Yong Baek Kim. Hard-core bosons on the kagome lattice: Valence-bond solids and their quantum melting. *Phys. Rev. Lett.*, 97:147202, Oct 2006.

[49] Arnab Sen, Kedar Damle, and T. Senthil. Superfluid insulator transitions of hard-core bosons on the checkerboard lattice. *Phys. Rev. B*, 76:235107, Dec 2007.

[50] Jie Lou, Anders Sandvik, and Naoki Kawashima. Antiferromagnetic to valence-bond-solid transitions in two-dimensional SU(n) heisenberg models with multi-spin interactions. *Phys. Rev. B*, 80:180414, Nov 2009.

[51] Kenji Harada, Naoki Kawashima, and Matthias Troyer. Néel and spin-peierls ground states of two-dimensional $su(n)$ quantum antiferromagnets. *Phys. Rev. Lett.*, 90(11):117203, Mar 2003.

[52] Ribhu K. Kaul. Marshall-positive SU(n) quantum spin systems and classical loop models: A practical strategy to design sign-problem-free spin hamiltonians. *Phys. Rev. B*, 91:054413, Feb 2015.

[53] K. S. D. Beach, Fabien Alet, Matthieu Mambrini, and Sylvain Capponi. SU(n) heisenberg model on the square lattice: A continuous-n quantum monte carlo study. *Phys. Rev. B*, 80:184401, Nov 2009.

[54] Matthew S. Block, Roger G. Melko, and Ribhu K. Kaul. Fate of $\mathbb{CP}^{N-1}$ fixed points with q monopoles. *Phys. Rev. Lett.*, 111:137202, Sep 2013.

[55] Ribhu K. Kaul. Quantum phase transitions in bilayer su(n) antiferromagnets. *Phys. Rev. B*, 85:180411, May 2012.

[56] Adam Nahum, J. T. Chalker, P. Serna, M. Ortuño, and A. M. Somoza. 3d loop models and the cp^{n-1} sigma model. *Phys. Rev. Lett.*, 107:110601, Sep 2011.

[57] D'Emidio J. and R. K. Kaul. New $\mathbb{CP}^{N-1}$ fixed points. *https://arxiv.org/abs/1610.07702*, 2016.

[58] Ganpathy Murthy and Subir Sachdev. Action of hedgehog-instantons in the disordered phase of the 2+1 dimensional cp^{N-1} model. *Nucl. Phys. B*, 344:557, 1990.

[59] Ethan Dyer, Márk Mezei, Silviu S. Pufu, and Subir Sachdev. Scaling dimensions of monopole operators in the $\mathbb{CP}^{N-1}$ theory in $2+1$ dimensions. *Journal of High Energy Physics*, 2015(6):1–48, 2015.

[60] Ribhu K. Kaul and Subir Sachdev. Quantum criticality of u(1) gauge theories with fermionic and bosonic matter in two spatial dimensions. *Phys. Rev. B*, 77(15):155105, Apr 2008.

[61] Adam Nahum, J. T. Chalker, P. Serna, M. Ortuño, and A. M. Somoza. Deconfined quantum criticality, scaling violations, and classical loop models. *Phys. Rev. X*, 5:041048, Dec 2015.

[62] Igor Herbut. *A Modern Approach to Critical Phenomena.* Cambridge University Press, 2010.

[63] S. Kolnberger and R. Folk. Critical fluctuations in superconductors. *Phys. Rev. B*, 41:4083–4088, Mar 1990.

[64] I. F. Herbut and Z. Tešanović. Herbut and tešanović reply:. *Phys. Rev. Lett.*, 78:980–980, Feb 1997.

[65] Kenji Harada. Bayesian inference in the scaling analysis of critical phenomena. *Phys. Rev. E*, 84:056704, Nov 2011.

[66] Kenji Harada. Kernel method for corrections to scaling. *Phys. Rev. E*, 92:012106, Jul 2015.

[67] Sheer El-Showk, Miguel F. Paulos, David Poland, Slava Rychkov, David Simmons-Duffin, and Alessandro Vichi. Solving the 3d ising model with the conformal bootstrap. *Phys. Rev. D*, 86:025022, Jul 2012.

[68] Ansgar Dorneich and Matthias Troyer. Accessing the dynamics of large many-particle systems using the stochastic series expansion. *Phys. Rev. E*, 64:066701, Nov 2001.

[69] M.E. Peskin and D.V. Schroeder. *An Introduction to Quantum Field Theory.* Advanced book classics. Addison-Wesley Publishing Company, 1995.

[70] P. M. Chaikin and T. C. Lubensky. *Principles of Condensed Matter Physics.* Cambridge University Press, 2000.

Vita

JONATHAN D'EMIDIO

Education

University of Kentucky, Lexington, Kentucky
Thesis advisor: Professor Ribhu K. Kaul
Research Focus: Quantum criticality in SU(N) spin models using Monte Carlo
M.S. in Physics (2014)

The Pennsylvania State University, State College, PA
B.S. in Physics, B.A. in French, B.A. in International Studies, Minor in Math (2010)

Professional Experience

- **Graduate Teaching Assistant,** University of Kentucky (Fall 2010 – Spring 2012)
- **Graduate Research Assistant,** University of Kentucky (Fall 2012 – Spring 2017)

Publications

1. Jonathan D'Emidio, Ribhu K. Kaul. *New easy-plane* $\mathbb{CP}^{N-1}$ *fixed points*, Phys. Rev. Lett. **118**, 187202 (2017).
2. Jonathan D'Emidio, Simon Lovell, Ribhu K. Kaul. *Quadrupolar quantum criticality on a fractal*, arXiv:1708.07924 (2017).
3. Jonathan D'Emidio, Ribhu K. Kaul. *First-order superfluid to valence-bond solid phase transitions in easy-plane SU(N) magnets for small N*, Phys. Rev. B **93**, 054406 (2016).
4. Jonathan D'Emidio, Matthew S. Block, Ribhu K. Kaul. *Rényi entanglement entropy of critical SU(N) spin chains*, Phys. Rev. B **92**, 054411 (2015).

Awards

- Keith B. MacAdam graduate excellence scholarship (July 2016 - July 2017).